

MICROMACHINED SCANNING DEVICES FOR 3D ACOUSTIC IMAGING

A Dissertation

by

CHIH-HSIEN HUANG

Submitted to the Office of Graduate and Professional Studies of
Texas A&M University
in partial fulfillment of the requirements for the degree of

DOCTOR OF PHILOSOPHY

Chair of Committee,	Jun Zou
Committee Members,	Chin B. Su
	Arum Han
	Sheng-Jen Hsieh
Head of Department,	Miroslav M. Begovic

August 2015

Major Subject: Electrical Engineering

Copyright 2015 Chih-Hsien Huang

ABSTRACT

Acoustic imaging (including ultrasound and photoacoustic imaging) refers to a class of imaging methods that use high-frequency sound (ultrasound) waves to generate contrast images for the interrogated media. It provides 3D spatial distribution of structural, mechanical, and even compositional properties in different materials. To conduct 3D ultrasound imaging, 2D ultrasound transducer arrays followed by multi-channel high-frequency data acquisition (DAQ) systems are frequently used. However, as the quantity and density of the transducer elements and also the DAQ channels increase, the acoustic imaging system becomes complex, bulky, expensive, and also power consuming. This situation is especially true for 3D imaging systems, where a 2D transducer array with hundreds or even thousands of elements could be involved.

To address this issue, the objective of this research is to achieve new micromachined scanning devices to enable fast and versatile 2D ultrasound signal acquisition for 3D image reconstruction without involving complex physical transducer arrays and DAQ electronics. The new micromachined scanning devices studied in this research include 1) a water-immersible scanning mirror microsystem, 2) a micromechanical scanning transducer, and 3) a multi-layer linear transducer array. Especially, the water-immersible scanning mirror microsystem is capable of scanning focused ultrasound beam (from a single-element transducer) in two dimensions for 3D high-resolution acoustic microscopy. The micromechanical scanning transducer is capable of sending and receiving ultrasound signal from a single-element transducer to a 2D array of locations for 3D acoustic tomography. The multi-layer linear transducer

array allows a unique electronic scanning scheme to simulate the functioning of a much larger 2D transducer array for 3D acoustic tomography. The design, fabrication and testing of the above three devices have been successfully accomplished and their applications in 3D acoustic microscopy and tomography have been demonstrated.

DEDICATION

for my parents

Yao-Yuan and Xuan-Qing

and my wife Yun-Hui

ACKNOWLEDGEMENTS

Foremost, I would like to express my profound gratitude to my committee chair, Dr. Jun Zou, who provides scientific guidance in my research and exchanges valuable life experience.

I am also thankful to my committee members, Dr. Chin B. Su, Dr. Sheng-Jen Hsieh, and Dr. Arum Han for their constructive comments and supports throughout the course of this research.

My appreciation also goes to my friend and colleague, Dr. Cheng-Chung Chang, for sharing research experiences and his broad knowledge in optics and imaging. His expertise helps me to create useful designs and to conduct meaningful experiments in this work.

I also want to extend my gratitude to the technical staff of Aggie Fab. I would like to thank Mr. Robert Atkins, Mr. Jim Gardner, Mr. Dennie Spears, and Mr. Larry Rehn for maintaining a good working environment and functional equipment.

Thanks also go to my friends and colleagues in solid state group and Washington University at Saint Louis. Dr. Yi-Chen Lo, Dr. Po-Chun Chen, and Dr. Jun-Jie Yao shared their invaluable experiences in device fabrication and photoacoustic imaging. Mr. Hu He and Mr. Young Cho provided supports and training for the clean room and laser machining equipment.

Last but most importantly, I would like to thank my parents and my wife for their continuously support and encouragement. Without their support, this work would not be possible and accomplished.

NOMENCLATURE

MEMS	Microelectromechanical systems
ORPAM	Optical resolution photoacoustic microscopy
PA	Photoacoustic
PAT	Photoacoustic tomography
PAM	Photoacoustic microscopy
PVDF	Polyvinylidene fluoride
SAM	Scanning acoustic microscopy
SAFT	Synthetic aperture focusing technique
SNR	Signal to noise ratio

TABLE OF CONTENTS

	Page
ABSTRACT	ii
DEDICATION	iv
ACKNOWLEDGEMENTS	v
NOMENCLATURE.....	vi
TABLE OF CONTENTS	vii
LIST OF FIGURES.....	ix
LIST OF TABLES	xii
1. INTRODUCTION.....	1
1.1 Motivation.....	1
1.2 Summary of Work	2
2. WATER-IMMERSIBLE SCANNING MIRROR MICROSYSTEM FOR ACOUSTIC MICROSCOPY*	4
2.1 Introduction.....	4
2.2 Design and Fabrication	6
2.2.1 Design.....	6
2.2.2 Fabrication.....	12
2.3 Characterization.....	13
2.4 Ultrasound Microscopy Experiment.....	17
2.5 Applications in Photoacoustic Microscopy.....	20
3. MICROMECHANICAL SCANNING TRANSDUCER FOR ACOUSTIC TOMOGRAPHY	23
3.1 Introduction.....	23
3.2 Device Concept and Feasibility Study	24
3.2.1 Device Concept	24
3.2.2 Feasibility Study.....	26
3.3 Design, Construction and Characterization	31
3.3.1 Design and Construction	31
3.3.2 Scanning Characterization.....	37
3.4 Data Acquisition and Image Reconstruction	38

3.4.1	Data Acquisition.....	38
3.4.2	Image Reconstruction.....	40
3.5	Imaging Experiments and Results	44
3.5.1	Alignment of the Detection Points	45
3.5.2	Image Reconstruction.....	47
4.	MULTI-LAYER TRANSDUCER ARRAY FOR ACOUSTIC TOMOGRAPHY.....	52
4.1	Introduction.....	52
4.2	Device Concept and Feasibility Study.....	53
4.2.1	Device Concept	53
4.2.2	Feasibility Study.....	55
4.3	Design, Construction and Characterization	58
4.3.1	Design and Construction	58
4.3.2	Characterization.....	61
4.4	Data Acquisition and Image Reconstruction	65
4.4.1	Data Acquisition.....	65
4.4.2	Image Reconstruction.....	67
4.5	Imaging Experiment and Results.....	68
4.5.1	Experimental Setup	70
4.5.2	Imaging Results	70
5.	CONCLUSIONS AND FUTURE WORK	73
	REFERENCES	75
	APPENDIX MATLAB AND LABVIEW PROGRAMS	82

LIST OF FIGURES

	Page
Figure 2.1 Illustration of the underwater operation of micro scanning mirrors in (a) pulse-echo ultrasound and (b) photoacoustic microscopic imaging.....	6
Figure 2.2 Schematics of the water-immersible scanning mirror design: (a) side view; (b) top view of fast-axis module; and (c) top view of slow-axis module. PM, permanent magnets; PF, polymer frame; AF, actuation force; AH, acrylic holder.....	8
Figure 2.3 A fully assembled prototype of the water-immersible scanning mirror.....	13
Figure 2.4 Illustration of laser tracing method.....	15
Figure 2.5 Scanning angles of the fast axis of the water-immersible scanning mirror: (a) With a DC driving voltage; and (b) With an AC at the resonance frequency in air (224 Hz) and water (164 Hz). CW, clockwise; CCW, counter clockwise.....	16
Figure 2.6 Scanning angles of the slow axis of the water-immersible scanning mirror: (a) With a DC driving voltage; and (b) With an AC at the resonance frequency in air (55 Hz) and water (38Hz). CW, clockwise; CCW, counter clockwise.....	17
Figure 2.7 (a) Schematic setup of the pulse/echo ultrasound microscopic imaging setup; and (b) Averaged peak-to-peak voltage of the backscattered ultrasound signal as a function of lateral and vertical scanning location....	19
Figure 2.8 Schematic of MEMS-OR-PAM. CL, condenser lens; AC, aluminum coating; AL, acoustic lens; UT, ultrasonic transducer.....	21
Figure 2.9 MEMS-OR-PAM of blood flow dynamics of the vasculature in a mouse ear. Capillaries were clearly resolved, and the flow dynamics over a $2 \times 5 \text{ mm}^2$ area were imaged with a 0.8 Hz volumetric frame rate and 400 Hz B-scan rate.....	22
Figure 2.10 MEMS-OR-PAM of flow dynamics of carbon particles. (a) MEMS OR-PAM image of a mouse ear with a pulse energy of 100 nJ, where the blood vessels were imaged. (b) After the injection of carbon particles via the tail vein, a smaller region indicated by the dashed box in (a) was monitored with a 4 Hz volumetric frame rate. The pulse energy was reduced to 10 nJ to image only the particles. The dashed	

lines are the boundaries of the vessel containing the flowing particles. A representative particle is indicated by the arrows.	22
Figure 3.1 Comparison of different patterns for single element ultrasound transducer scanning system	26
Figure 3.2 Schematic of co-register imaging experiment.	28
Figure 3.3 Scanning path of linear translation stages.....	28
Figure 3.4 Layouts of imaging samples, experiments, and pixels of 2D pattern	29
Figure 3.5 A-Scan results when (a) laser pulse illuminated target, and (b) ultrasound pulse reflected by target.	30
Figure 3.6 3D imaging reconstruction results of co-register imaging experiments.	30
Figure 3.7 (a) Schematic of the 2-axis micromechanical scanning transducer design. (b) Picture of the constructed prototype.....	33
Figure 3.8 (a) Waveforms of the two AC driving signals and ultrasound pulses. (b) The resulting distribution of ultrasound detection points on a circular scanning path. (c) Picture of the optical trace of a LED-illuminated optical fiber tip driven by the two-axis microactuator....	35
Figure 3.9 The scanning angle as a function of the AC driving voltage.....	38
Figure 3.10 Schematic of the data acquisition system. CHA and CHB are the input channels and EXT is the external trigger channel of the DAQ card.....	40
Figure 3.11 3D Image reconstruction process. (a) Circular B-Scan image reconstruction. (b) Sector B-Scan image reconstruction. (c) C-Scan image slicing. (d) 3D image formation.....	41
Figure 3.12 Illustration of the geometry for the calculation of the observation distance for SAFT. (a) on circular planes. (b) on sector planes.....	43
Figure 3.13 Picture of the imaging target.....	44
Figure 3.14 (a) Random time delay in the AC driving signals and the resulting misalignment of the ultrasound detection points. (b) Re-alignment of the ultrasound detection points based on the AC driving signals.	46
Figure 3.15 B-Scan image of a representative circular plane (a) before and (b) after applying SAFT. B-Scan image of a representative sector plane (c) before and (d) after applying SAFT.	48

Figure 3.16 Reconstructed 3D ultrasound images in Volview. (a) Raw image. (b) Image with white margin removed. (c) Image with white margin removed and after applying SAFT. The red, green and blue lines indicate the x y and z axes.	50
Figure 4.1 2D Image reconstruction process. (a) Schematic of laser spot on top of two transducer arrays (line: 1D array at the top, dot: 1D array at the bottom.) (b) Imaging results of horizontal 1D array. (c)Imaging results of vertical 1D array. (d) Reconstructed 2D image.	54
Figure 4.2 (a) System setup of feasibility study experiment. (b) Traveling path of single element transducer. (c) Top view of imaging sample.	56
Figure 4.3 (a) 3D imaging result of signals from 16x16 locations. (b) 3D imaging result of signals from 16 plus 16 rectangular locations.	57
Figure 4.4 (a) Schematic of the transducer array and pads design. (b) Schematic of the common ground side and its pad. (c) Illustration of two 1D transducer arrays bonded together. (d) Picture of 2D PVDF transducer array.	60
Figure 4.5 Setup of frequency characterization experiment (a) and the results for different targets including (b) rubber tape, (c) hex wrench, and (d) pencil lead.....	62
Figure 4.6 Results of ultrasound sensitivity experiment of (a) top layer and (b) bottom layer.....	64
Figure 4.7 (a) Schematic of the data acquisition system. (b) Received ultrasound signals before (Top) and after (Bottom) multiplexer IC.	66
Figure 4.8 Simulation of (a) A-Scan results from 16 channels ultrasound transducer array which aligned along x direction. (b)A-Scan results from 16 channels ultrasound transducer array which aligned along y direction. (c) B-Scan result of x direction ultrasound array (Top) and y direction ultrasound array (Bottom). (d) 3D B-Scan image of direction ultrasound array (Top) and y direction ultrasound array (Bottom). (e) Result of 3D imaging reconstruction.	68
Figure 4.9 (a) Alignment of imaging targets and (b) Picture of the imaging target.....	69
Figure 4.10 Picture of 3D imaging reconstruction experiment.	70
Figure 4.11 B-Scan image of 1D transducer arrays (a) top layer (b) bottom layer and (c) the result of 3D imaging reconstruction.	71

LIST OF TABLES

	Page
Table 2.1 Design parameters of the fast-axis module.	10
Table 2.2 Design parameters of slow-axis module.	11
Table 2.3 Estimated driving angles and resonance frequencies.	11

1. INTRODUCTION

1.1 Motivation

Acoustic imaging (including ultrasound and photoacoustic imaging) refers to a class of imaging methods that use high-frequency sound (ultrasound) waves to generate contrast images for the interrogated media [1, 2]. It provides the spatial distribution of structural, mechanical, and even compositional properties in different materials.

Therefore, it has become a useful non-destructive diagnostic technique with a wide range of applications. Depending on the number of dimensions of the imaged region, acoustic imaging can be divided into 2D or 3D. The 2D imaging generates a cross-sectional (B-Scan) image of the imaging target, while the 3D imaging creates a volumetric (3D) visualization, which is easier to interpret than a B-Scan image. Therefore, 3D ultrasound imaging is able to provide diagnostic information with higher quality and quantity than 2D ultrasound imaging [3-11].

To conduct 3D ultrasound imaging, the time-serial ultrasound signals from a 2D array of locations on the imaging target has to be properly received for 3D image reconstruction. To achieve this, a 2D ultrasound transducer array followed by a multi-channel high-frequency data acquisition (DAQ) system is often used [12-19]. The imaging performance (e.g., resolution, field of view, and data collection speed) is determined by the number and density of the transducer elements and the number of the DAQ channels [20-23]. However, as the number and density of the transducer elements increase, the fabrication and packaging of the transducer array becomes more challenging. To interface each transducer element, a large number of high-frequency

DAQ channels are required, which makes the ultrasound imaging system complex, bulky, expensive and also power consuming. This situation is especially true for 3D imaging systems, where a 2D transducer array with hundreds or even thousands of elements could be involved. This situation not only sets a practical limit on the maximal number of DAQ channels and thus the performance of a 3D imaging system, but also prevents the development of low-cost, low-power and ultraportable ones suitable for field operations. To address this issue, the objective of this research is to study new micromachined scanning devices to enable fast and versatile 2D ultrasound signal acquisition, such as 3D acoustic imaging can be achieved without involving complex physical transducer arrays and DAQ electronics. The new micromachined scanning devices studied in this research include 1) a water-immersible scanning mirror microsystem for 3D acoustic microscopy, 2) a micromechanical scanning transducer for 3D acoustic tomography, and 3) a multi-layer transducer array for 3D acoustic tomography. An outline of the details of this research is described as follows.

1.2 Summary of Work

As discussed in Chapter 2, a new water-immersible scanning mirror microsystem has been designed, fabricated and tested. To achieve reliable underwater operation, flexible polymer torsion hinges were used to support the reflective mirror plate. Energy efficient electromagnetic microactuators were constructed to drive the mirror plate around a fast axis and a slow axis. The performance of this water-immersible scanning mirror microsystem in both air and water were tested using the laser tracing method. The feasibility of using such a water-immersible scanning mirror microsystem for scanning

ultrasound microscopic imaging has successfully been demonstrated. The water-immersible scanning mirror microsystem has been used to build a high-speed and high-resolution photoacoustic microscopic imaging system. Its application in the in-vivo functional imaging of biological tissues is also described.

As discussed in Chapter, a new two-axis micromechanical scanning transducer has been designed, fabricated and tested. It consists of a miniaturized single-element ultrasound transducer driven by a compact 2-axis liquid-immersible electromagnetic microactuator. It is capable of sending and receiving ultrasound signals over a 2D array of locations, whose density and arrangement are controlled by software programming. Therefore, it can be used to simulate any virtual 2D transducer array with any density and arrangement of its elements. Using the scanning transducer, 3D ultrasound tomography was successfully demonstrated with only one channel of data acquisition (DAQ) electronics. The lateral resolution of the 3D ultrasound image was further improved with the synthetic aperture focusing technique (SAFT).

As discussed in Chapter 4, a new multi-layer transducer array has been designed, fabricated and tested. It consists of two 1D linear arrays of line transducers positioned orthogonally to each other. They were used to provide electronic scanning to generate two orthogonal 2D B-Scan images (x/z and y/z), respectively. A 3D ultrasound tomographic image was successfully reconstructed from the two 2D B-Scan images. Therefore, the multi-layer transducer array technique makes it possible to use $2 \times N$ transducer elements and DAQ channels to simulate 3D imaging with $N \times N$ transducer elements and DAQ channels.

2. WATER-IMMERSIBLE SCANNING MIRROR MICROSYSTEM FOR ACOUSTIC MICROSCOPY*

2.1 Introduction

Scanning mirrors have been used in a number of high-resolution optical imaging modalities, including optical coherence tomography [24, 25], confocal microscopy [26] and multi-photon microscopy [27]. Compared with conventional scanning mirrors [28], MEMS (microelectromechanical systems) scanning mirrors have a smaller form factor and is able to provide higher scanning speeds. They are especially suitable for developing compact imaging probes for handheld, endoscopic and even intravascular applications. Currently, MEMS scanning mirrors are mainly designed for free-space optical beam steering in air, where the mirror supporting structure is made of brittle silicon-based material and the mirror is driven by delicate microactuators [28]. However, these designs are not suitable for underwater scanning operations in ultrasound [29] and photoacoustic imaging [30-33], where water is usually the matching medium for acoustic propagation (Fig. 2.1). For example, when immersed in water, the silicon supporting structures are susceptible to permanent damage from a small turbulence,

*@ 2013 Springer. Reprinted with permission from Chih-Hsien Huang, Junjie Yao, Lihong Wang, and Jun Zou, "A water-immersible 2-axis scanning mirror microsystem for ultrasound and photoacoustic microscopic imaging applications," *Microsyst Technol* (2013) 19: 577–582. doi: 10.1007/s00542-012-1660-4

*@ 2012 SPIE. Reprinted, with permission, from Chih-Hsien Huang, Lidai Wang, Joon-Mo Yang, Liang Gao, Konstantin I. Maslov, Jun Zou, and Lihong V. Wang "Wide-field fast-scanning photoacoustic microscopy based on a water-immersible MEMS scanning mirror," *Journal of Biomedical Optics*, Aug. 2012, Vol. 17(8), pp. 1-3.

shock or unbalanced surface tension force, which otherwise are often encountered in a liquid environment. Second, significant degradation in the scanning performance (e.g., maximal scanning angle and frequency) or complete device failure could possibly occur due to electrical shorting, excessive cooling and fluidic damping. To address this issue, we report the development of a new water-immersible scanning mirror microsystem, which is able to operate reliably in both air and water. By utilizing high-strength polymer supporting materials and efficient electromagnetic microactuators, fast scanning of both optical and high-frequency ultrasonic beams in water has been successfully achieved. This new capability could enable the development of compact ultrasonic and photoacoustic microscopic imaging systems with fast imaging speed and large field of view.

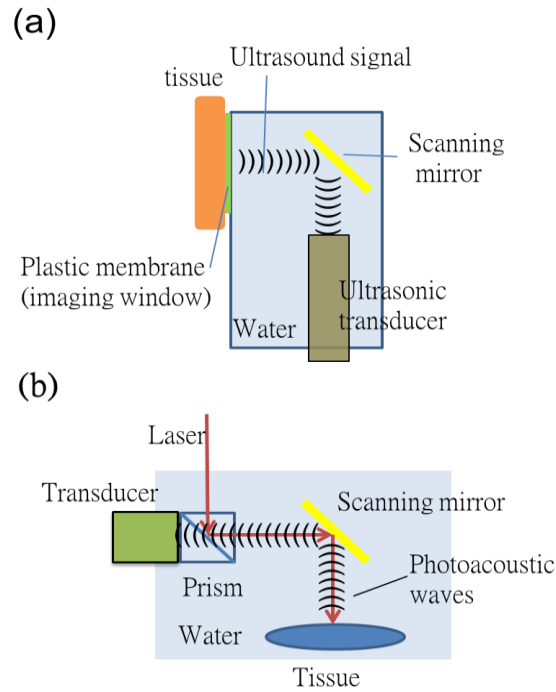


Figure 2.1 Illustration of the underwater operation of micro scanning mirrors in (a) pulse-echo ultrasound and (b) photoacoustic microscopic imaging

2.2 Design and Fabrication

2.2.1 Design

Fig. 2.2(a) shows the schematic design of the water-immersible scanning mirror, which consists of a fast-axis module and a slow-axis module. The reflective mirror plate is housed in the fast-axis module and supported by two micro torsion hinges made of high-strength BOPET (biaxially-oriented polyethylene terephthalate) film. The low stiffness and high fracture strain of the polymer hinges help to reduce the required driving force and minimize the chance of shock damage [28]. Electromagnetic actuation was chosen as the driving mechanism to enable reliable underwater scanning. Compared

with other microactuation mechanisms, such as electrostatic, piezoelectric and thermal methods, electromagnetic actuation does not need high voltage or electro-heating, and therefore is more suitable in a liquid environment. Compact electromagnetic actuation was achieved by combining a single inductor coil with two micro rare-earth magnet discs attached to the two ends of the mirror plate with opposite polarities. When an AC or DC current flows through the inductor coil, the resultant magnetic field creates a torque on the magnets and thus rotates the mirror plate around the torsional supporting hinges. To achieve the second (slow) axis scanning, the fast-axis module is attached to the slow-axis module with the support of two BOPET torsional hinges (Fig. 2.2(b)). Four inductor coils and four micro rare-earth magnet discs were arranged into two groups with opposite polarities to provide the torsional driving force for the slow-axis scanning. Due to its larger mass, the resonant frequency of the slow-axis module will be lower than the fast-axis module. One advantage of the above modular design is that scanning motion in the two axes is largely decoupled, which helps to improve the scanning accuracy, linearity and repeatability.

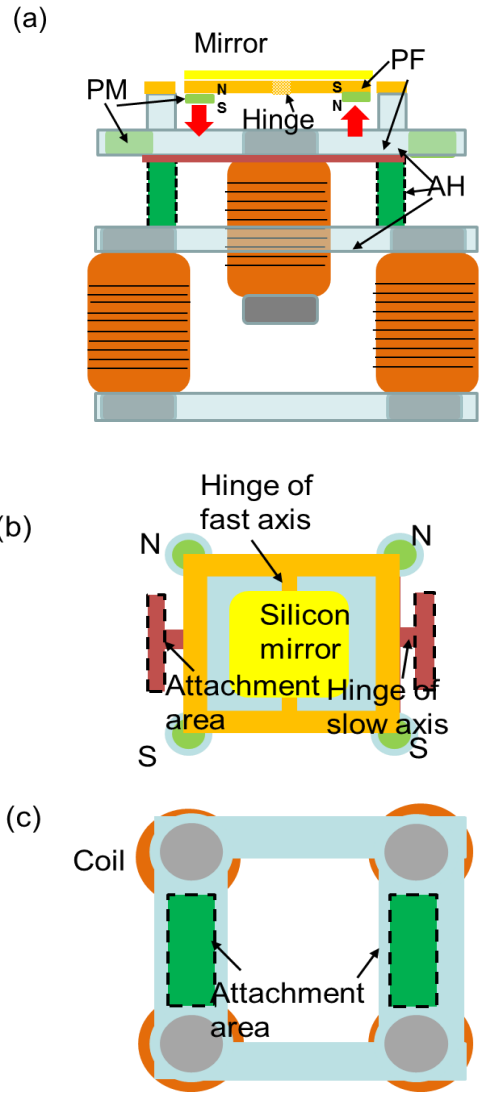


Figure 2.2 Schematics of the water-immersible scanning mirror design: (a) side view; (b) top view of fast-axis module; and (c) top view of slow-axis module. PM, permanent magnets; PF, polymer frame; AF, actuation force; AH, acrylic holder.

In ultrasound and photoacoustic imaging, the optical and ultrasound signals are in the form of short pulses with a typical repetition rate of kHz. To maintain a dense pixel formation, the scanning frequency of the scanning mirror should be 10s to 100s of Hz. A maximal scanning angle larger than 10° is desirable to provide a good field of

view. To ensure a good numerical aperture, the size of the mirror plate should be as large as possible. In addition, the driving voltage needed to be minimized to reduce the risk of electrical shorting and shock especially in water. Tables 2.1 and 2.2 list the main design parameters of the fast-axis and slow-axis module. Based on these design parameters, a preliminary mechanical analysis was conducted to provide a first-order estimation of their scanning performances (scanning angle, resonant frequency and driving voltage). The magnetic force (F) generated between the permanent magnet discs and the inductor coil can be determined by

$$F = V \times Ms \times \frac{\partial H}{\partial z} \quad (2.1)$$

where V is the volume of permanent magnetic disc, Ms is the magnetization of the magnet disc. H is the magnetic field intensity generated by inductor. The torque T_{mag} generated by the magnetic force and the resulting rotation angle (ϕ) can be determined by

$$T_{mag} = F \times L' \quad (2.2)$$

$$\phi = \frac{TL}{JG} \quad (2.3)$$

where L , J and G are the length, torsional moment of inertia and shear modulus of elasticity of the BOPET hinges, respectively and L' is the work distance between the magnetic force (F) and the BOPET hinges. For the BOPET hinge with a rectangular cross-section, the torsion moment of inertia (J) can be determined by

$$J = wt^3 \left[\frac{16}{3} - 3.36 \frac{t}{w} \left(1 - \frac{t^4}{12w^4} \right) \right] \quad (2.4)$$

where w is the width and t is the thickness of the BOPET hinge. The resonant frequency in air (f_{r_air}) of the fast-axis and the slow-axis modules can be estimated by

$$f_{r_air} = \frac{1}{2\pi} \sqrt{\frac{K^*}{m}} \quad (2.5)$$

where K^* is the torsional force constant of the BOPET hinge and m is the overall effective mass of the fast-axis and the slow-axis modules, respectively. Due to the small movement of the mirror plate during scanning and the relatively large mass of the two modules, the damping from the air is allowed to be neglected. When the scanning mirror is immersed in water, the resonant frequency (f_{r_water}) is estimated by

$$f_{r_water} = f_{r_air} \sqrt{1 + \frac{3\pi\rho b}{2\rho_m t'}}^{-1} \Gamma_t(\kappa) \quad (2.6)$$

where ρ is the density of water, ρ_m and b are the effective density and width of the scanning mass, $\Gamma_t(\kappa)$ is hydrodynamic functions, and κ is normalized mode numbers [34]. From Eqs. (1) to (9), the estimated scanning angles and resonant frequencies of the fast-axis and slow-axis modules are listed in Table 2.3.

Table 2.1 Design parameters of the fast-axis module.

Inductor		Neodymium Magnets	
Inductance	33mH	Thickness	0.8 mm
		Diameter	3.125 mm
Mirror Plate		Supporting Hinge	
Length	9 mm	Length	1 mm
Width	9 mm	Width	0.9 mm
Thickness	500 μ m	Thickness	75 μ m

Table 2.2 Design parameters of slow-axis module.

Inductor		Neodymium Magnets	
Inductance	33 mH	Thickness	1.6 mm
		Diameter	3.125 mm
Mirror Plate		Supporting Hinge	
Length	9 mm	Length	1 mm
Width	9 mm	Width	1.4 mm
Thickness	500 μm	Thickness	75 μm

Table 2.3 Estimated driving angles and resonance frequencies.

	Fast axis		Slow axis
ϕ (DC 16V)	12.8°	ϕ (DC 10V)	7.88°
Fr_{air}	214.38 Hz	Fr_{air}	63.92 Hz
Fr_{water}	160.06 Hz	Fr_{water}	45.24 Hz

2.2.2 Fabrication

The fabrication of the water-immersible scanning mirror was conducted as follows. First, the reflective mirror plate ($9 \times 9 \text{ mm}^2$) was diced from a polished single-crystalline silicon substrate. The polished silicon substrate provides excellent surface smoothness and flatness, and also good acoustic reflectivity due to the large acoustic impedance mismatch between silicon ($19.6 \times 10^6 \text{ N} \cdot \text{s}/\text{m}^3$) and water ($1.47 \times 10^6 \text{ N} \cdot \text{s}/\text{m}^3$). A thin layer of gold coating ($\sim 70 \text{ nm}$ thick) was deposited onto the silicon mirror surface using e-beam evaporation to enhance its optical reflectivity. Second, the BOPET torsional hinges and acrylic holders of both fast-axis and slow-axis modules were made by a laser cutting machine. During the assembly, the silicon mirror plate, the BOPET torsional hinges, the permanent magnet discs (D21B-N52, K&J Magnetics), the inductor coil (70F331AF-RC, BOURNS) and the acrylic holder were assembled and bonded together with silicone rubber adhesive (RTV 108, Momentive Performance Materials) to form the fast-axis module. The same procedure was repeated to make the slow-axis module. Finally, the fast-axis module was bonded onto the acrylic holder of the slow-axis module (see Fig. 2.2). After insulating the coils and electrical connections, the entire 2-D scanning mirror module can be immersed in water to ensure a reliable underwater scanning operation (Fig. 2.3).

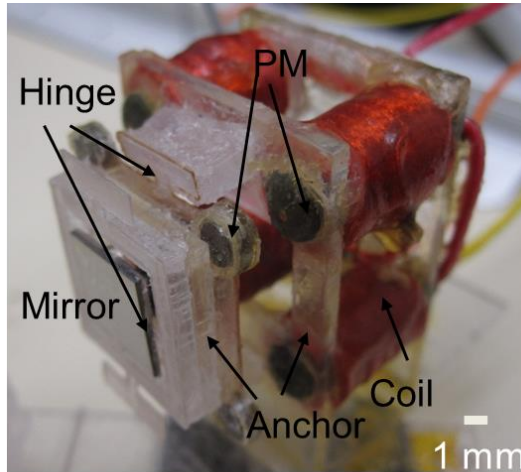


Figure 2.3 A fully assembled prototype of the water-immersible scanning mirror.

2.3 Characterization

The scanning angle ϕ and resonance frequency f_r of the scanning mirror were measured in air and water by using the laser tracing method (Fig. 2.4). During the measurement, the scanning mirror was mounted on the bottom of a water tank. A ruler was placed 6.5 cm away from the center of the mirror plate at an angle of 45° . The laser beam from a laser pointer was projected onto the mirror plate with an incident angle of 45° and reflected onto the ruler. The scanning angle was calculated based on the trace of the laser beam on the ruler. To determine the resonance frequency, an AC driving voltage with varied frequency was applied. The resonance frequency is defined as the frequency of the AC driving voltage when the scanning angle reaches its maximum. Fig. 2.5 shows the scanning angles of the fast axis under DC and AC driving conditions. As shown in Fig. 2.5(a), under DC driving condition, the scanning angle increased with the driving voltage in both directions (clockwise (CW) and counter-clockwise (CCW)). The

scanning angle reached 12° with a 16 V driving voltage, which matches well with the estimated value. The scanning angles of the fast axis were similar in air and water. This is because the mirror plate was driven in a quasi-static mode and the dynamic damping from water can be negligible. As shown in Fig. 2.5(b), with AC driving at the resonance frequency, the scanning angle increased with the peak driving voltage in both air and water. However, due to the dynamic damping in water, the resonance frequency drops from 224 Hz in air to 164 Hz in water, which is similar to the estimation results and higher driving voltage is needed to maintain the same scanning angle. For example, at a scanning angle of 10° , the required peak driving voltage increased from 7.5 V in air to 10 V in water. The scanning performance of the slow axis of the scanning mirror was also characterized. As shown in Fig. 2.6(a), under DC driving condition, the scanning angle reached 6.5° with a 10 V driving voltage in both air and water. The resonant frequency dropped from 55 Hz in air to 38 Hz in water. With an AC driving voltage of 10 volt (at 55 Hz in air and 38 Hz in water), the scanning angle dropped from 8.5° in air to 6° in water as shown in Fig. 2.6(b). The estimated rotation angle and resonance frequencies of slow axis are not accurate as fast axis since the structure of the slow axis is much more complex, which is well described by a lumped-element model. In addition, as a reliability test, the fast axis of the scanning mirror was driven in water with a peak driving voltage of 10 V and a frequency of 164 Hz for over ten million cycles. No noticeable degradation in the scanning performance was observed.

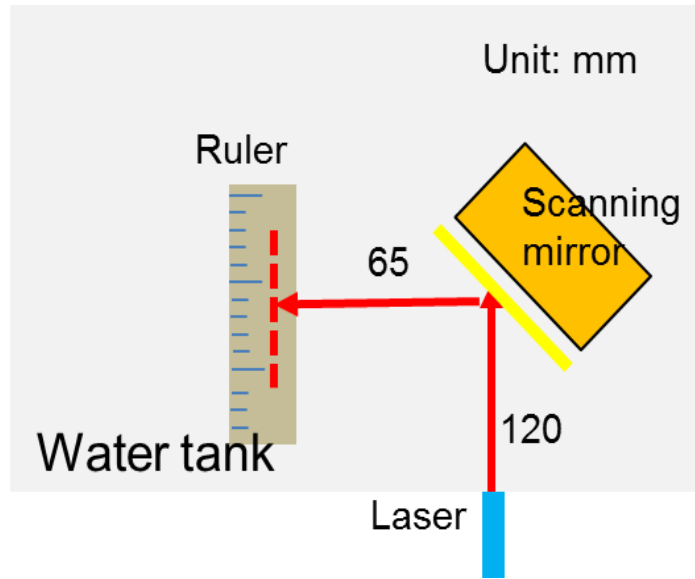


Figure 2.4 Illustration of laser tracing method.

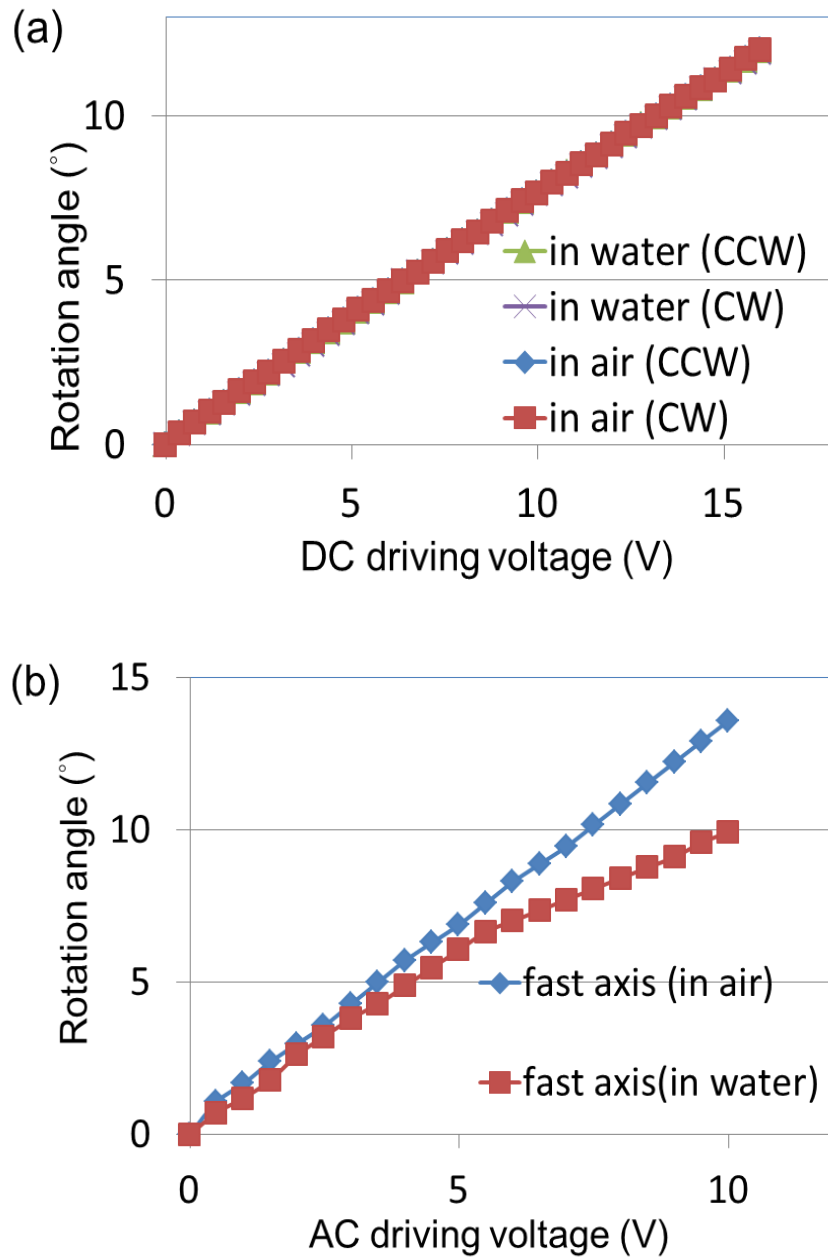


Figure 2.5 Scanning angles of the fast axis of the water-immersible scanning mirror: (a) With a DC driving voltage; and (b) With an AC at the resonance frequency in air (224 Hz) and water (164 Hz). CW, clockwise; CCW, counter clockwise.

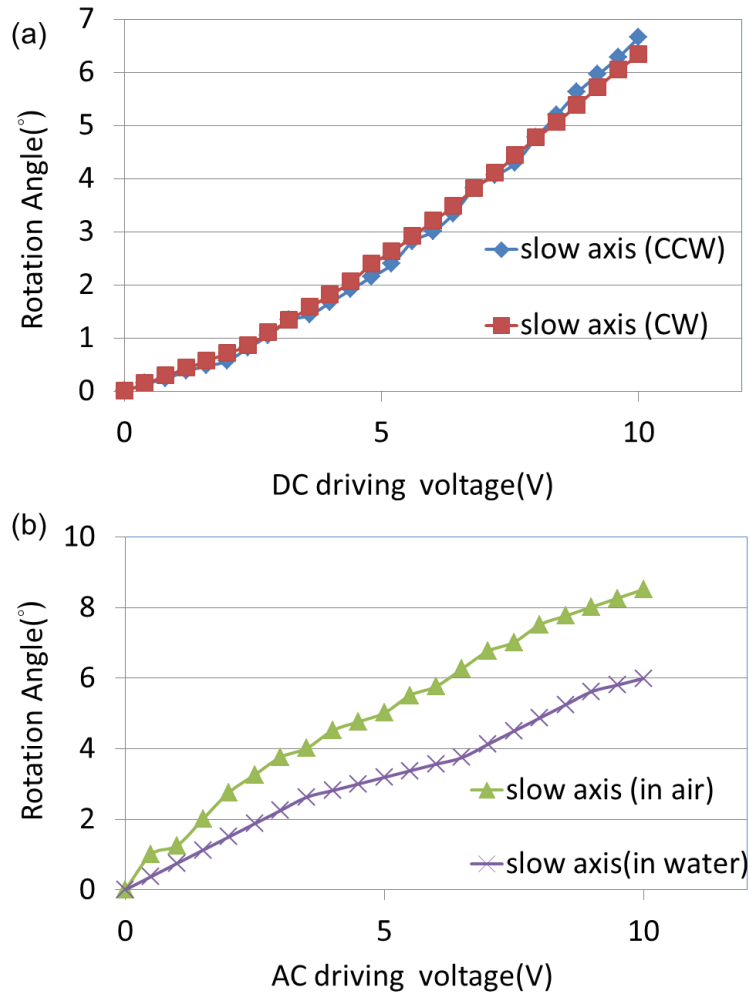


Figure 2.6 Scanning angles of the slow axis of the water-immersible scanning mirror: (a) With a DC driving voltage; and (b) With an AC at the resonance frequency in air (55 Hz) and water (38Hz). CW, clockwise; CCW, counter clockwise.

2.4 Ultrasound Microscopy Experiment

Using the water-immersible scanning mirror to steer focused ultrasound beam in water, pulse-echo ultrasound microscopic imaging of an optical-fiber target were successfully demonstrated. As shown in Fig. 2.7(a), the imaging setup includes a water tank, a high-frequency (25 MHz) focused transducer with a focal length of 19 mm

(V324N-SU, Olympus), the water-immersible scanning mirror, and three optical fibers as the imaging target. The scanning mirror is placed 9 mm away from the transducer at an angle of 45° . The three optical fibers are placed 10 mm away from the center of the mirror plate, such that they are located in the focal zone of the ultrasound transducer. The diameter of the optical fibers is $140\ \mu\text{m}$ and the pitches between two adjacent fibers are 0.64 mm and 0.7 mm, respectively. The ultrasound transducer is connected to a pulser/receiver system (5072PR, Olympus) and an oscilloscope (TDX 2014B, Tektronix). The pulses repetition rate and pulse width were set to be 200 Hz and $1\ \mu\text{s}$, respectively. A DAQ card ((PCI 6251, National Instruments) and a custom-built operational amplifier array were used to provide DC voltages to drive the two axes of the scanning mirror. The DC driving voltage of the fast axis was from -10V to 10V with a 0.4V increment and that of the slow axis was from 0 to 8V with a 0.4V increment. This forms 1000 scanning steps, corresponding to a scanning area of $0.8\ \text{mm} \times 2.6\ \text{mm}$ with 20×50 pixels. At each “pixel”, the peak-to-peak voltage of the received ultrasound signals were measured and averaged 128 times. To automate the scanning and data acquisition process, a Labview (National Instruments) program was developed to control the DAQ card and the oscilloscope. Fig. 2.7(b) shows the normalized averaged peak-to-peak voltages as a function of the lateral and vertical scanning location. The distances between the three peaks of the backscattered ultrasound signals were 0.676 mm and 0.728 mm, respectively, which agreed well with the actual distances between the optical fibers.

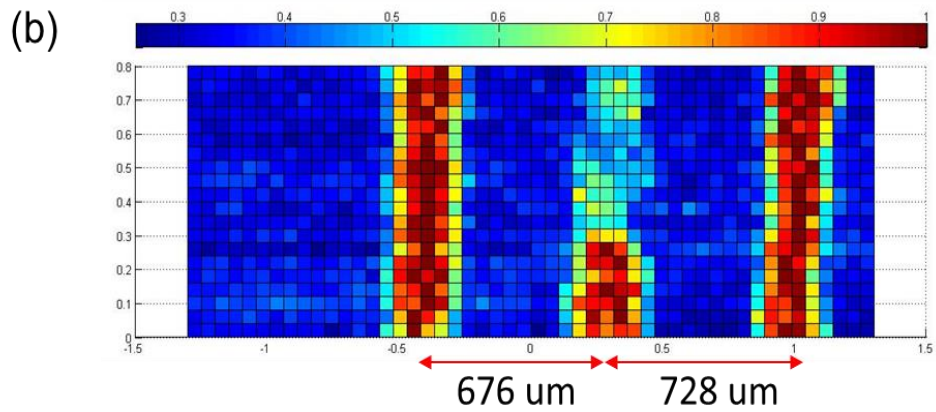
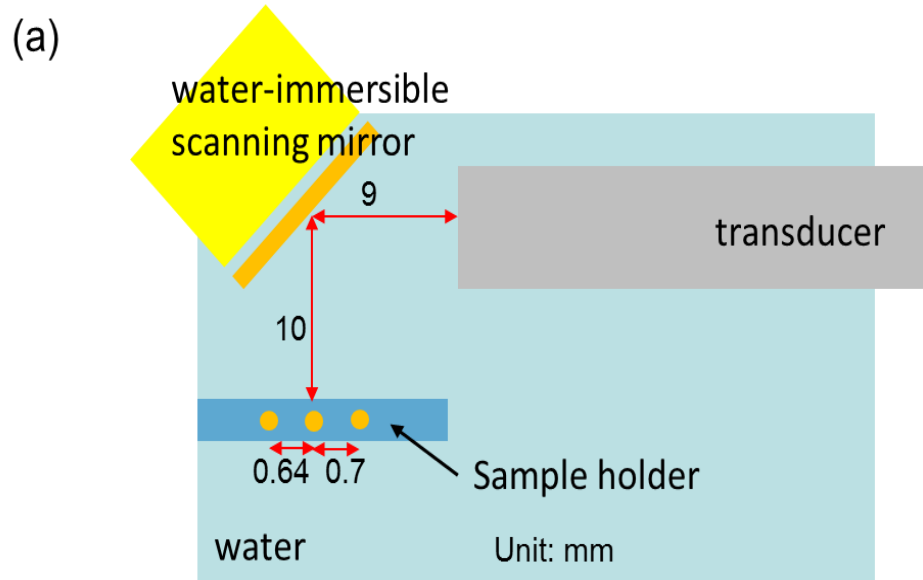


Figure 2.7 (a) Schematic setup of the pulse/echo ultrasound microscopic imaging setup; and (b) Averaged peak-to-peak voltage of the backscattered ultrasound signal as a function of lateral and vertical scanning location.

2.5 Applications in Photoacoustic Microscopy

A water-immersible microelectromechanical systems (MEMS) scanning mirror was used to build a wide-field fast-scanning OR-PAM (MEMS-OR-PAM) by collaborators in Washington University of Saint Louis to achieve cross-sectional (B-scan) image with 400 Hz imaging rate over a 3 mm range. In this system the laser beam and reflected ultrasound signal were both scanned as Fig. 2.8 shows. The light source is Nd:YVO₄ laser (AOT-YVO-100Q, AOT Inc.), the pulse duration is 2 ns and the wavelength is 532 nm with a repetition rate of 100 kHz. The laser beam was focused by a condenser lens (LA1131, Thorlabs) and filtered by a 50 μm diameter pinhole (P50C, Thorlabs). The filtered beam was focused by an optical objective lens (AC127-050-A, Thorlabs. NA: 0.1 in air). A beam combiner composed of an aluminum-coated prism (NT32-331, Edmund) and an uncoated prism (NT32- 330, Edmund) provides acoustic-optical coaxial alignment. The focused laser beam is directed toward the sample surface by the aluminum coated MEMS scanning mirror plate. Besides, the resultant photoacoustic waves were reflected by the MEMS scanning mirror and detected by an ultrasonic transducer (V214-BB-RM, Olympus-NDT) with central frequency of 50 MHz and a -6 dB bandwidth of 100%. The whole imaging head is submerged in a water tank for ultrasound coupling. Volumetric imaging is provided by fast angular scanning of the MEMS scanning mirror along the x-axis and linear translation scanning of the step motor along the y-axis. The dimension of silicon MEMS mirror plate in this application was 9 × 9 mm² with 500 μm thickness with an 80-nm-thick gold coating which provides

a good reflection of both the optical and acoustic beams and the supporting hinges was $1 \times 0.9 \text{ mm}^2$.

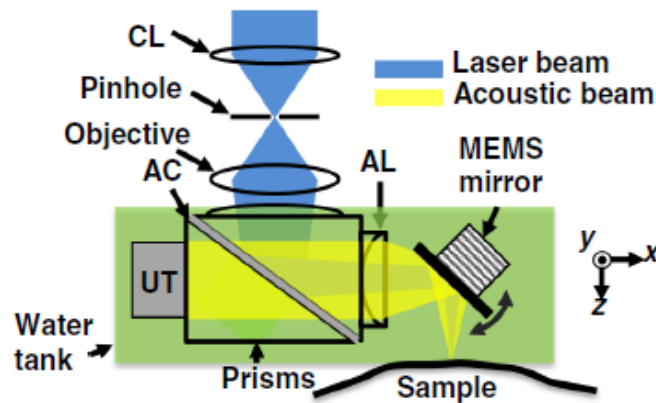


Figure 2.8 Schematic of MEMS-OR-PAM. CL, condenser lens; AC, aluminum coating; AL, acoustic lens; UT, ultrasonic transducer.

Imaging experiments were conducted by collaborators from Washington University of Saint Louis. First, Red blood cell (RBC) flow in a nude mouse ear was imaged in vivo by MEMS-OR-PAM to demonstrate its high-speed imaging capability. (Fig. 2.9) In addition to the RBC flow imaging, intravascular transport was also explored by using contrast agent (Fig. 2.9).

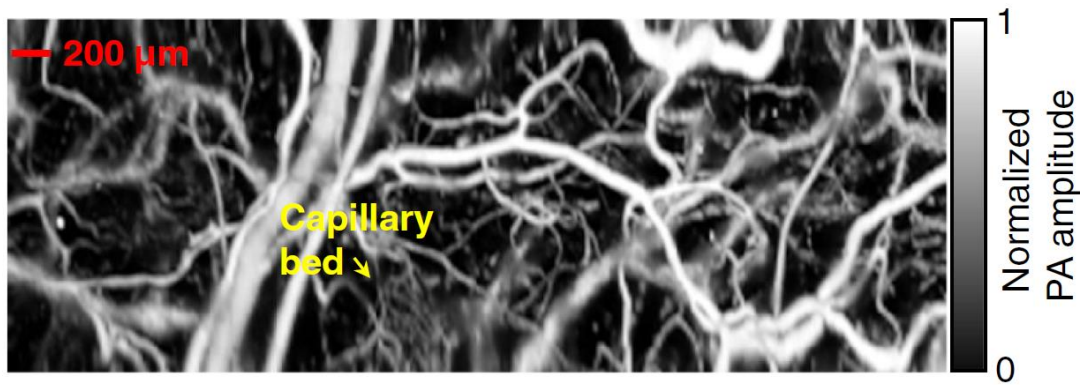


Figure 2.9 MEMS-OR-PAM of blood flow dynamics of the vasculature in a mouse ear. Capillaries were clearly resolved, and the flow dynamics over a $2 \times 5 \text{ mm}^2$ area were imaged with a 0.8 Hz volumetric frame rate and 400 Hz B-scan rate.

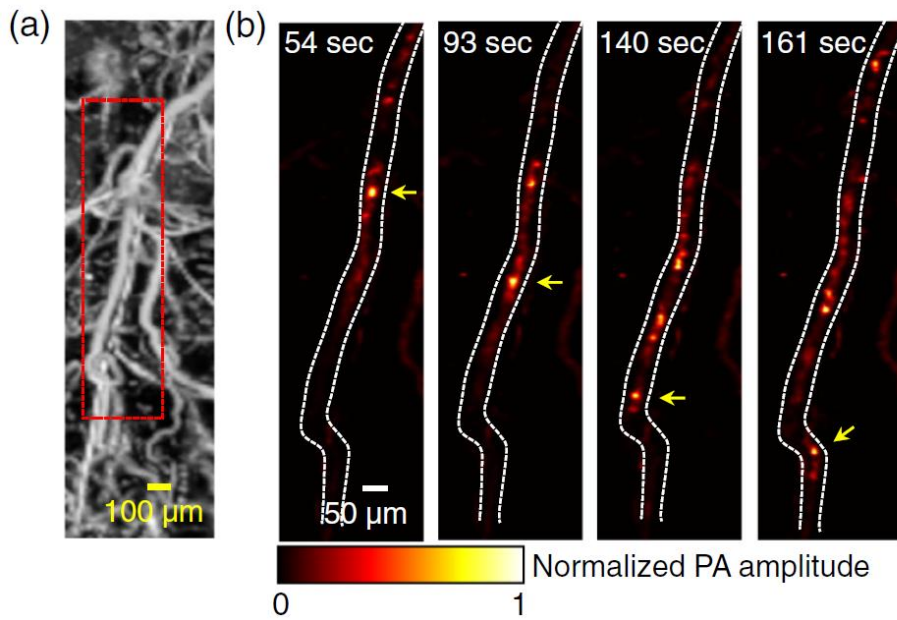


Figure 2.10 MEMS-OR-PAM of flow dynamics of carbon particles. (a) MEMS OR-PAM image of a mouse ear with a pulse energy of 100 nJ, where the blood vessels were imaged. (b) After the injection of carbon particles via the tail vein, a smaller region indicated by the dashed box in (a) was monitored with a 4 Hz volumetric frame rate. The pulse energy was reduced to 10 nJ to image only the particles. The dashed lines are the boundaries of the vessel containing the flowing particles. A representative particle is indicated by the arrows.

3. MICROMECHANICAL SCANNING TRANSDUCER FOR ACOUSTIC TOMOGRAPHY

3.1 Introduction

Ultrasound imaging (2D or 3D) has become a useful non-destructive diagnostic technique with a wide range of applications [35, 36]. To conduct 3D ultrasound imaging, the time-variant ultrasound field at a 2D array of locations has to be properly recorded for image reconstruction [2, 3, 8, 37]. Currently, there are three different methods to achieve 3D ultrasound imaging. First, a 2D ultrasound transducer array can be used to detect the incoming ultrasound signals in one or multiple transmission-receiving (T/R) cycles [14, 16, 38]. However, to obtain good imaging resolution and field-of-view, a large number (100s~1000s) of transducer elements and T/R channels are required. As a result, the entire imaging system could become complex, bulky, power-consuming, and expensive [39]. To address this issue, a 1D transducer array could be used to conduct “electronic” 2D B-Scan, while the scan in the azimuth dimension is conducted mechanically by using a one-axis motor stage or just by hand with the assistance of a position tracking device [5, 6, 9]. However, this method still requires an ultrasonic transducer array and multiple T/R channels. The need of a position tracking device complicates the imaging system design and operation [7, 10]. In addition, the data acquisition speed is also limited by the slow mechanical scanning and complex position tracking. Alternatively, the ultrasound signals can also be received by mechanically scanning a single-element transducer over the imaging target by using a two-axis motor stage. However, the use of 2-axis motor stages makes the entire imaging system complex

and bulky. Second, the slow mechanical scanning frequency limits the data acquisition speed. As a result, this technique is mainly limited for lab use and is not suitable for handheld operations [7, 10, 40, 41].

In this paper, we report a new 2-axis micromechanical scanning transducer technique to enable fast and versatile 3D ultrasound imaging. The 2-axis micromechanical scanning transducer consists of a miniaturized single-element transducer mounted a unique 2-axis water-immersible electromagnetic micro actuator. When AC driving currents are applied, the single-element transducer can be scanned along concentric paths with different radii at a frequency of 10s~100s Hz. By synchronizing the scanning frequency with the ultrasound pulse-echo repetition rate, the ultrasound signals from a 2D array of locations can be received sequentially with only one T/R channel for 3D image reconstruction. The two-axis micromechanical scanning transducer can be further miniaturized to be fitted into a liquid-filled compact probe for handheld operations. Therefore, it could provide a new approach for compact, fast and low-cost 3D ultrasound imaging systems.

3.2 Device Concept and Feasibility Study

3.2.1 Device Concept

Due to the complexity and high cost of using electronics to scan and receive ultrasound signals of 1D/2D transducer array, some researchers are working on using mechanical scanning strategies to scan single element transducer instead of electronic scanning devices and multi-elements transducer array. Fig. 3.1 indicates the possible scanning patterns of 2-axis single element ultrasound transducer mechanically scanning

systems. For systems without limitation of imaging speed, point by point scanning pattern are often used. For high speed imaging systems, most of them are using zigzag pattern with a fast axis and a slow axis. For 3D ultrasound imaging purpose, it is a common method to reconstruct a 3D image to stack several B-Scan images along x or y directions from results of zigzag 2D scan. However, a zigzag scanning system would require at least two hinges with different resonance frequencies. It is good for table top scanning systems, but would be too bulky and complex to build a handheld scanning transducer system with multi hinges. The most cost effective way would be have only one hinge and using coaxial cable of ultrasound transducer as main portion of the hinge. Since there is only one hinge, scanning the single element transducer along a circular or spiral pattern would be the best approach to achieve 2D scanning pattern as Fig. 3.1 shows. In order to evaluate the feasibility to reconstruct 3D imaging with circular pattern, a single element transducer scanning system was built with two linear translation stages (M-403.2DG, Physik Instrumente). Two silicon pieces and two pencil leads are used to build two imaging samples. Both samples are going to image by photoacoustic and ultrasound methodologies. This photoacoustic and ultrasound co-register 3D imaging experiment could also proof the potential of building a handheld imaging system with both 3D ultrasound and photoacoustic imaging abilities.

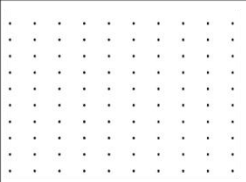
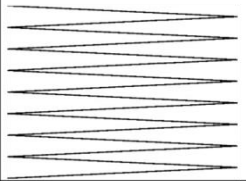
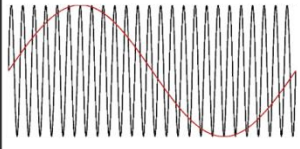
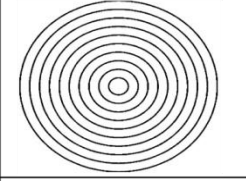
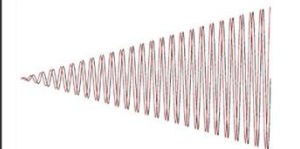
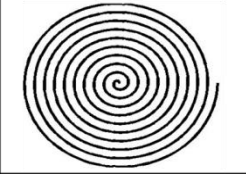
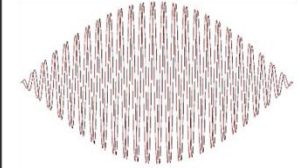
Scanning style	2-D pattern	Driving functions	Driving signals
Points by points		$x = a$ $y = b$	Several combinations of DC voltages
Zigzag		$x = \alpha \times \sin(t)$ $y = \beta \times \sin(t)$	
Circular		$x = r \times \sin(t)$ $y = r \times \cos(t)$	
Spiral		$x = \sin(r) \times \sin(t)$ $y = \sin(r) \times \cos(t)$	

Figure 3.1 Comparison of different patterns for single element ultrasound transducer scanning system

3.2.2 Feasibility Study

Fig. 3.2 shows the setup of co-register imaging experiment, a Q-switched Nd:YAG laser system was used to deliver laser pulses with a wavelength of 532 nm and a duration of 8 ns. The laser pulse was focused by an optical lens before introduce into a 220 um diameter optical fiber. The end of optical fiber was attached on a single element ultrasound transducer (XMS-310-B, Olympus) with center frequency of 10 MHz, 6-dB bandwidth of 80%, and diameter of 2 mm. The transducer was immersed into a water tank with imaging samples, and the distance between transducer and imaging targets

area is 5 mm. Two linear translation stages were used to carry the water tank and move along sector lines of circular paths. Fig. 3.3 indicates the scanning path of stacked translation stages with a paper stick on top of it and contact with a fixed pencil. Two imaging samples were consisted by two silicon pieces with 6 mm diameter and two pencil leads with 0.6 mm diameter respectively. Fig. 3.4 shows the construction of imaging samples, schematic of imaging experiments, and how to calculate the 2D scanning points. The step size represents the recording interval of DAQ card (AT9350-128M, Alazar Technologies), and the angle interval represents the angular difference between two linear scanning path. In photoacoustic imaging experiment, the laser pulse conducted to optical fiber and deliver to samples. The acoustic signals will be generated when laser pulse illuminated silicon pieces or pencil leads. In ultrasound imaging experiments, the ultrasound pulses were generate by pulser/receiver (5072PR, Olympus) through 10MHz transducer and the laser pulse didn't introduce into optical fiber. Both ultrasound and photoacoustic imaging experiments are using pulse laser as trigger signals to active the moving of linear translation stages and receiving acoustic signals through 10MHz transducer and pulser/receiver.

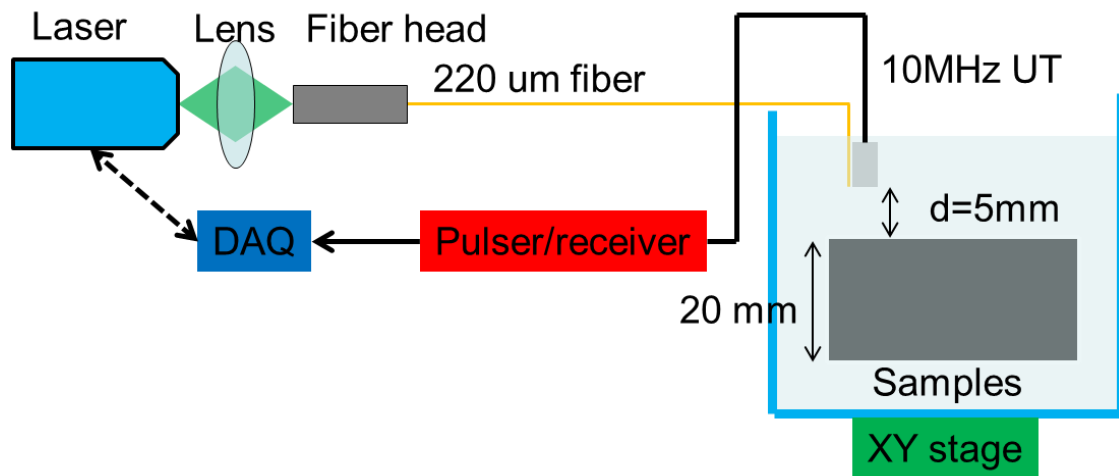


Figure 3.2 Schematic of co-register imaging experiment.

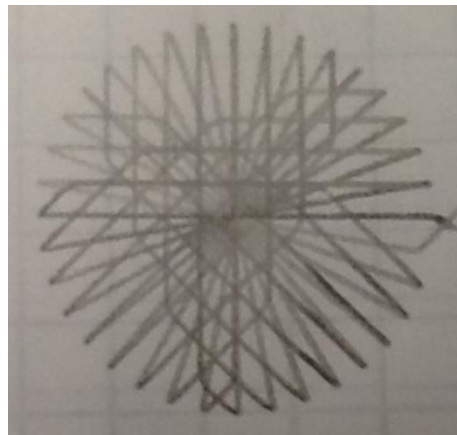


Figure 3.3 Scanning paths of linear translation stages.

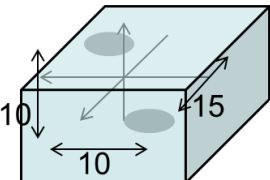
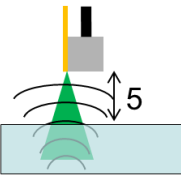
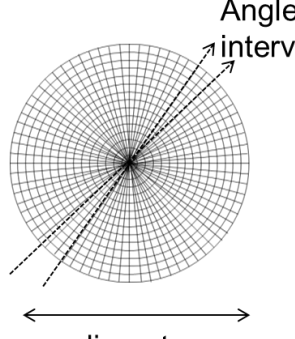
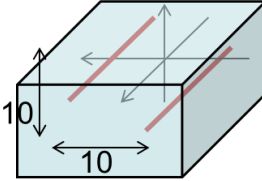
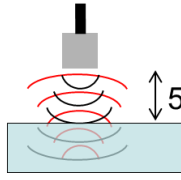
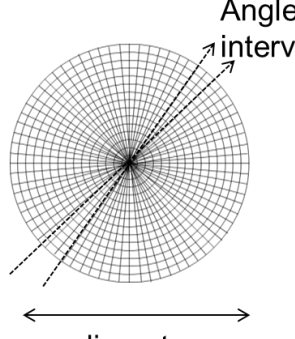
Sample	Imaging method	pixel
6 mm dia. Silicon Piece 	Photoacoustic 	$\frac{diameter}{Step\ int.} \times \frac{180}{Angle\ int.}$ 
0.6 mm dia. Pencil Lead 	Pulse/Echo 	

Figure 3.4 Layouts of imaging samples, experiments, and pixels of 2D pattern.

Fig. 3.5 shows the A-Scan results of photoacoustic imaging and pulse/echo imaging at the same positions where a silicon disc is under the single element transducer. The amplification (50dB) of both results is the same; it shows the signal strength of pulse/echo imaging was much stronger than photoacoustic imaging since the laser pulse was attenuated during introducing and transmission with an optical fiber. The results of 3D imaging reconstruction of different imaging methods and samples were showed in Fig. 3.6. The dynamic range of each image is the same and the results were agreed with the layout of imaging targets. The dimensions of silicon pieces were similar to real situation while in photoacoustic imaging experiments the reverberation effects happens due to the weaker signal strength. The width of pencil leads were larger than real

condition since the element size of transducer is 2mm and the maximum lateral resolution should be close to 1mm, which is, still larger than the real size of them.

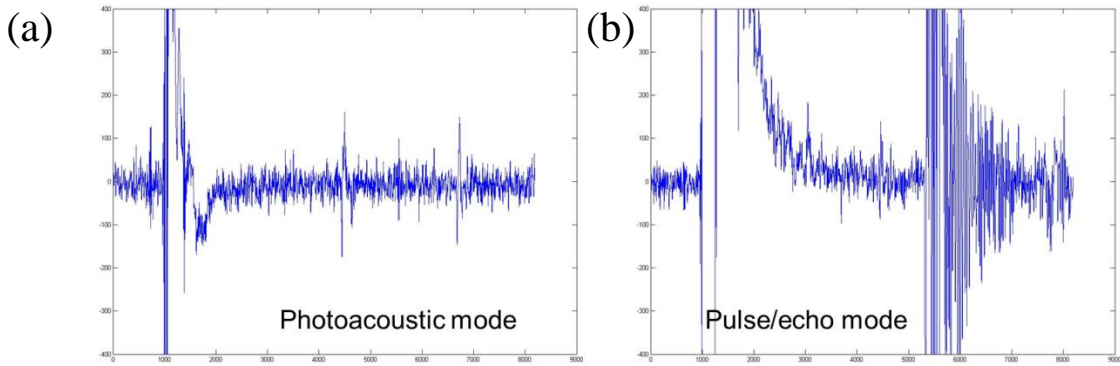


Figure 3.5 A-Scan results when (a) laser pulse illuminated target, and (b) ultrasound pulse reflected by target.

Sample	Imaging method	pixel	result
6 mm dia. Silicon Piece	Photoacoustic	$\frac{30}{0.3} \times \frac{180}{3} = 6000$	
6 mm dia. Silicon Piece	Pluse/Echo	$\frac{30}{0.3} \times \frac{180}{3} = 6000$	
0.6 mm dia. Pencil Lead	Photoacoustic	$\frac{30}{0.2} \times \frac{180}{3} = 9000$	
0.6 mm dia. Pencil Lead	Pluse/Echo	$\frac{30}{0.2} \times \frac{180}{3} = 9000$	

Figure 3.6 3D imaging reconstruction results of co-register imaging experiments.

3.3 Design, Construction and Characterization

3.3.1 Design and Construction

According to the preliminary research above, using circular path to conduct 3D imaging is possible. However, to enable useful 3D ultrasound imaging, fast scanning of the single-element transducer in two axes is needed. Since ultrasound waves with a frequency in the MHz range have high attenuation in air, a liquid coupling medium (oftentimes water) is needed for their effective propagation. Therefore, a micro actuator that is able to work properly under water is necessary. Currently, the most commonly used micro actuators are piezoelectric actuators. However, they require high driving voltages (e.g., >100 V), which could easily cause electrical breakdown or shorting in water. Their work distance is also very limited. In contrast, electromagnetic actuators do not need a high voltage to drive, which are suitable for working in a liquid environment. Besides, they generate large driving force at a large driving distance. Therefore, electromagnetic actuation will be chosen as the driving mechanism for the scanning transducer.

Fig. 3.7(a) shows the schematic design of the 2-axis micromechanical scanning transducer. A miniaturized single-element transducer is fixed onto a flexible hinge structure with a small permanent magnet attached onto it. To provide the driving force for scanning the transducer in two axes, two pairs of inductor coils are mounted close to the permanent magnet. The magnetic polarity of the two inductor coils in each pair is made opposite. When an AC current is flowing through the two inductor coils, a push and a pull force will be generated on the permanent magnet to vibrate the flexible hinge

together with the transducer at a certain scanning angle (θ). The vibration can be described as a simple harmonic motion. Its resonance frequency is related to the overall stiffness of the hinge, the mass of the magnet and transducer, and also the damping force encountered by the entire assembly. Fig. 3.7(b) shows the constructed prototype of the 2-axis micromechanical scanning transducer. A miniaturized water-immersion single-element transducer (XMS-310-B, Olympus) was used as the scanning transducer. It has a center frequency of 10 MHz, a 6-dB bandwidth of 80%, and a diameter of 2 mm. The RF coaxial cable of the single-element transducer was directly used as the supporting hinge, which was clamped onto a height adjustable stage. A neodymium ring magnet (R84X0, K&J Magnetics) was used as the permanent magnet. It has a length of 10 mm, an outer diameter of 5 mm, and an inner diameter of 2 mm, respectively. Its nominal peak magnetic field intensity is ~ 13200 Gauss. Eight RF coil inductors (70F331AF-RC, Bourns) were used as the driving coils. The inductance of each inductor is 330 mH. To provide good driving force, two inductors were connected in parallel. The use of two smaller coils instead of one larger coil results in a more compact structure and more uniform field distribution. The inductors and their wire connections were coated with water-proof epoxy. All the components were assembled together with acrylic fixtures made by laser cutting.

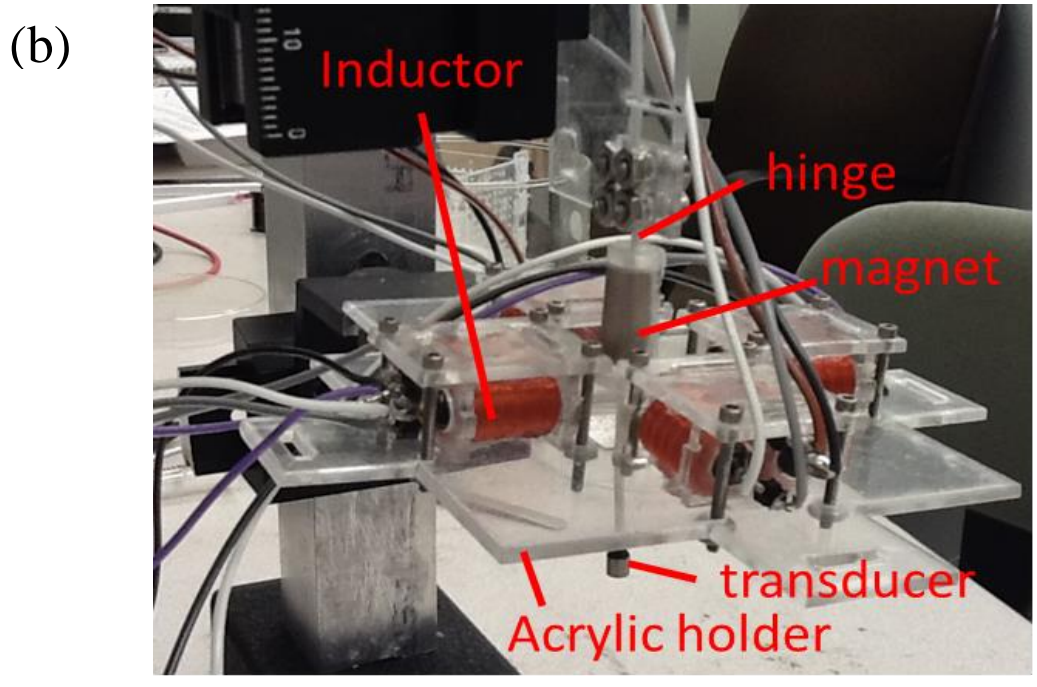
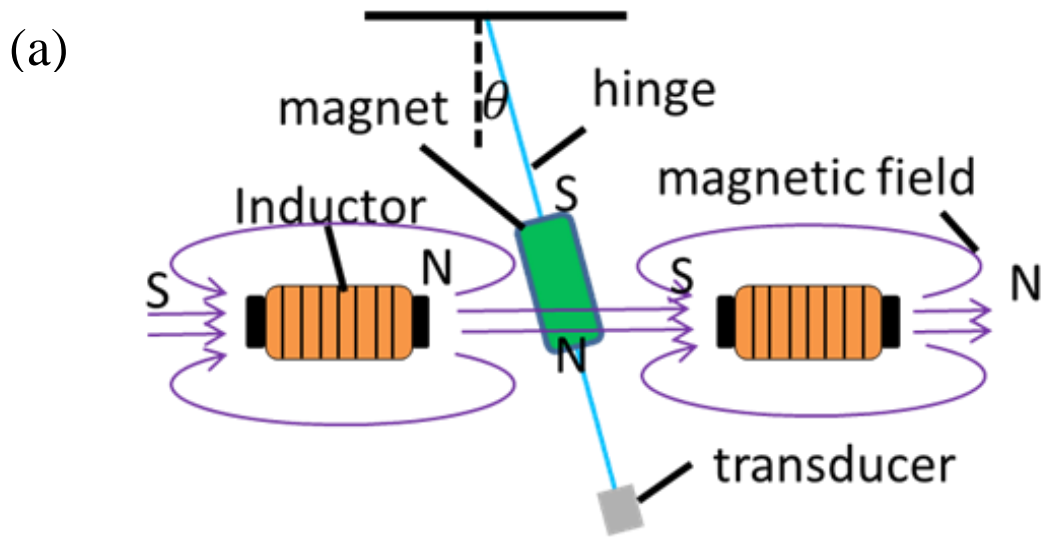


Figure 3.7 (a) Schematic of the 2-axis micromechanical scanning transducer design. (b) Picture of the constructed prototype.

When the frequency of the AC driving current matches the resonant frequency, θ reaches its maximum, which results in the most efficient driving condition. Due to its centrosymmetric structure, the resonant frequencies in both axes will be identical. Therefore, an ideal 2D scanning pattern will be a circular path (clockwise or counterclockwise), where both axes are driven at their resonant frequency [42-44]. As shown in Fig. 3.8(a), to generate a circular scanning path, the two AC driving currents must follow

$$I_x(t) = A \cos(\omega_r t) = A \cos(2\pi f_r t) \quad (3.1)$$

$$I_y(t) = A \sin(\omega_r t) = A \sin(2\pi f_r t) \quad (3.2)$$

where A is the amplitude of the driving currents and f_r is the resonant frequency of the hinge and transducer assembly [42, 45-47]. By adjusting the amplitude of the driving currents, the transducer can be scanned along one circular path with different radius (r), which is proportional to A (Fig. 3.8(b)). The location of the transducer at a certain time t_i can be represented as $(r\cos(\omega_r t_i), r\sin(\omega_r t_i))$. To dynamically configure the location of the detection points on each circular path, the mechanical scanning of the transducer needs to be synchronized with the ultrasound pulse repetition rate (f_u). The ratio between f_u and f_r will determine the effective number of detection points on each circular path.

The time interval (Δt) between two adjacent detection points will be the repetition period of the ultrasound pulses. The relative location of each detection point along on the circular path can be determined sequentially along with the driving signal. To demonstrate the two-axis scanning, the optical trace of a LED-illuminated optical fiber tip driven by the two-axis microactuator is shown in Fig. 3.8(c). In this work, the total

number of detection points on one circular path was set be 256. With an ultrasound pulse repetition rate of 5 kHz, the resonant frequency will need to be adjusted to 19.5315 Hz. For the data acquisition, after 256 A-Scan signals and driving signals are recorded, the scanning of the transducer will be moved onto a different circular path by adjusting the amplitude of the driving signal. The data recording will start again after a delay period (τ).[48]

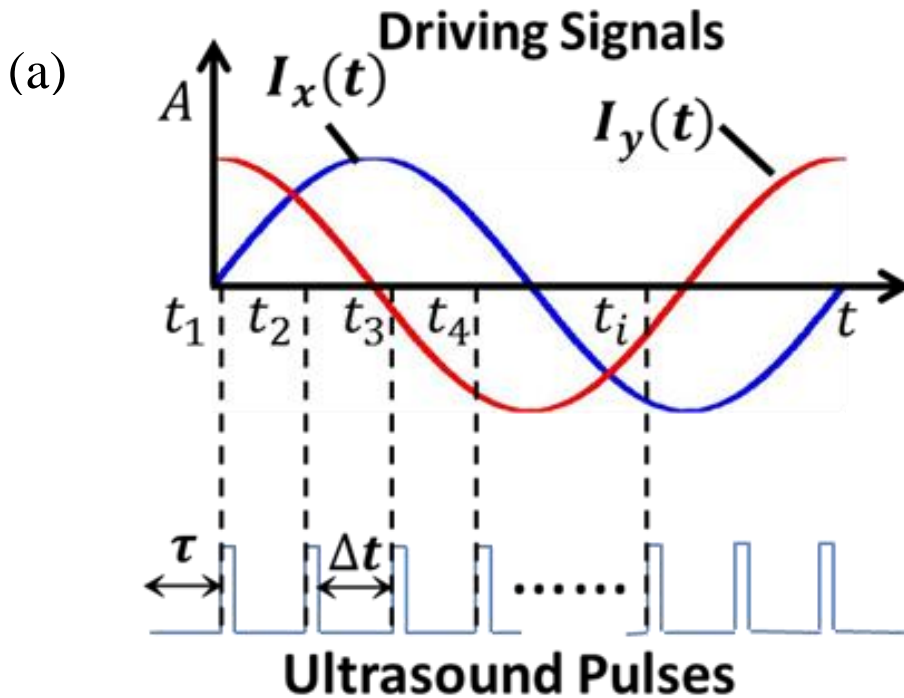
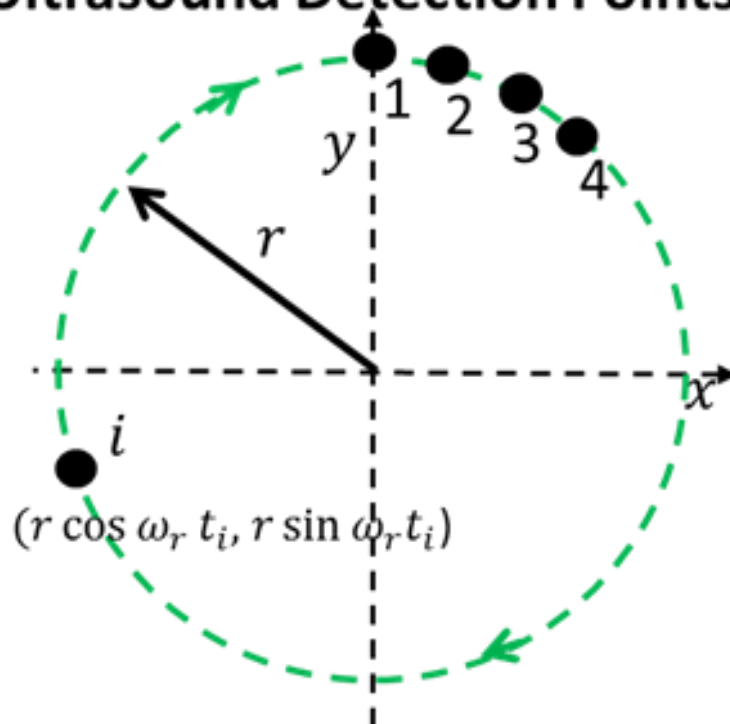


Figure 3.8 (a) Waveforms of the two AC driving signals and ultrasound pulses. (b) The resulting distribution of ultrasound detection points on a circular scanning path. (c) Picture of the optical trace of a LED-illuminated optical fiber tip driven by the two-axis microactuator.

(b) **Ultrasound Detection Points**



(c)

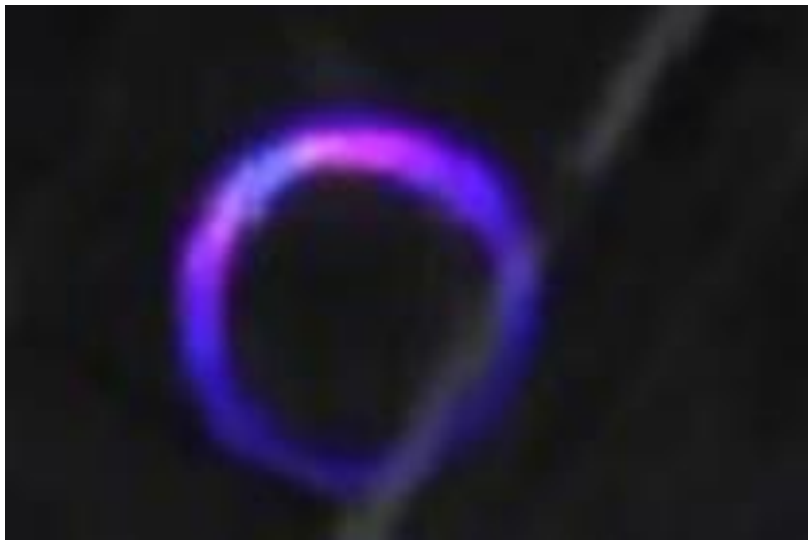


Figure 3.8 Continued.

3.3.2 Scanning Characterization

The entire scanning transducer setup was immersed in water to characterize the scanning angle when different driving currents were applied. Two function generators (33220A, 33220B, Agilent) were used to generate two AC signals at a frequency of 19.532 Hz, which have the same amplitude but with a phase difference of 90° . They were further amplified by two home-made current amplifiers before being sent to the inductor coils. Since the impedance of the inductors remains constant under the same frequency, the voltages applied on the inductors should be proportional to the currents flowing into them. Therefore, during the scanning characterization, the AC voltage drop on the inductor coils was monitored as a measure of the strength of the driving signals. Before the characterization of the scanning angle was conducted, the resonant frequency of the scanning transducer setup was fine-tuned to around 19.5 Hz. A driving voltage of 2.5 V (peak to peak) was applied onto the inductor coils. The length of the supporting hinge was carefully adjusted, so that the scanning angle reached its maximum. Next, the driving voltage was swept from 0 to 5 V (peak to peak) with an increment of 0.1 V. The amplitude of the vibration of the transducer was recorded and the scanning angle was calculated accordingly. The characterization was repeated on both axes. As shown in Fig. 3.9, the scanning angle changes almost linearly with the driving voltage. During the imaging experiment, this linear relationship was employed to determine the amplitude of the driving voltage to control the radius of a circular scanning path.

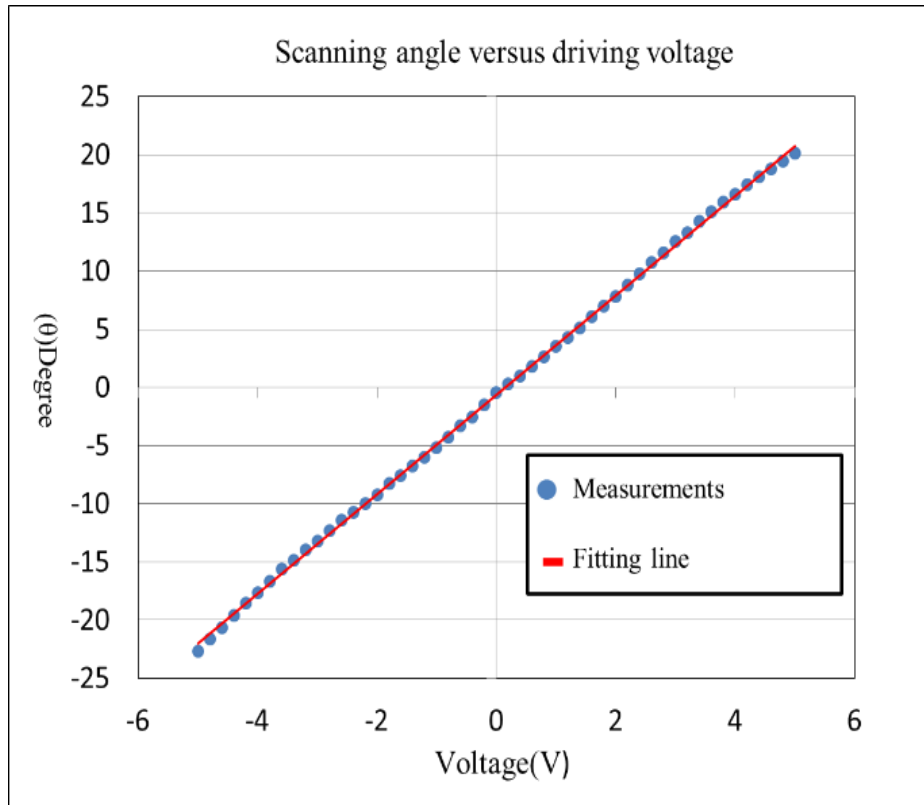


Figure 3.9 Scanning angle as a function of the AC driving voltage.

3.4 Data Acquisition and Image Reconstruction

3.4.1 Data Acquisition.

A schematic of the data acquisition system is shown in Fig. 3.10. The pulser-receiver (5072PR, Olympus) was set to provide a pulse repetition rate of 5 kHz, an amplification of 50 dB, and a damping ratio of 20 ohm. A personal computer loaded with LabView (version 2013, National Instruments) was used to trigger the two function generators (33220A, 33220B, Agilent) to generate two 19.532 Hz sinusoidal driving signals with 90° phase shift. After being amplified by the current amplifiers, the two

driving currents were sent to the scanning actuator to create a circular scanning path of the transducer. The diameter of each circular path is determined by the amplitude of the driving currents or voltages (Fig. 3.9). To form a 3D image with 60×256 detection points, the transducer was scanned on 60 circular paths with equal intervals. The external trigger port of the DAQ card (AT9350-128M, Alazar Technologies) was connected to the synchronization output port of pulser-receiver. Once being triggered by the pulser-receiver, it will start the data collection with 100 MHz sampling rate and 8192 sampling points. At each detection point, both the amplified ultrasound echo signals (from the pulser-receiver) and the driving signals from the function generator were recorded. For each ultrasound signal, all the 8192 sampling points were saved. For each driving signal, since all the 8192 sampling points have the same values, only the first sampling point was saved. Due to the short time interval ($\sim \mu\text{s}$) of the pulse-echo cycle, the location of the scanning transducer at each detection point can be considered static. After the data from all the 256 detection points on one circular path were recorded, the amplitude of the two driving currents was adjusted to move the transducer onto the next one. In the end, a total of $60 \times 256 \times 8192$ sampling points for the ultrasound signals and 60×256 sampling points for the driving signals were acquired and saved on the computer for image reconstruction.

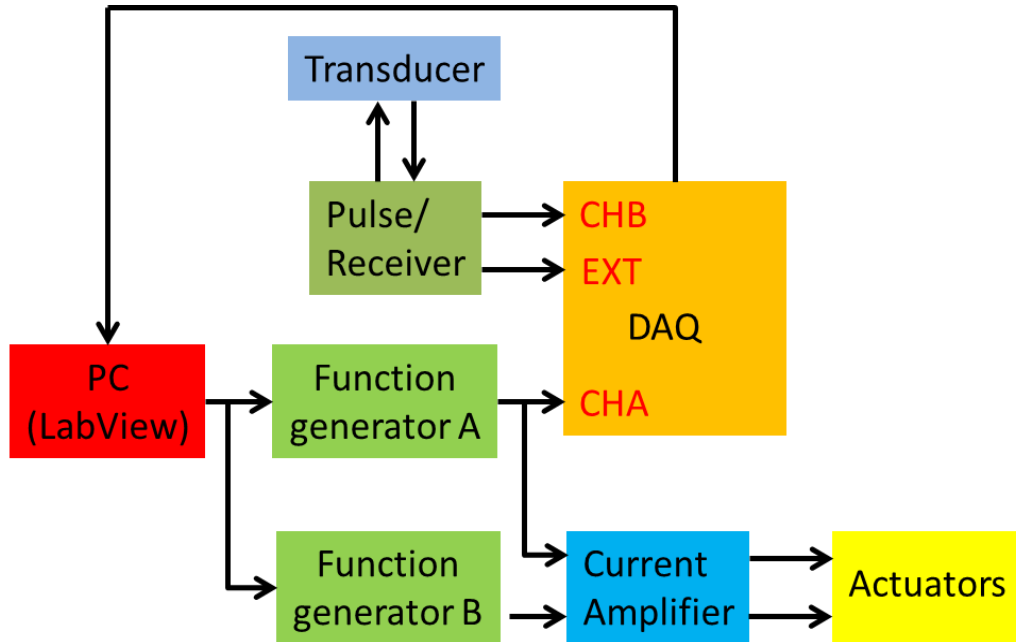


Figure 3.10 Schematic of the data acquisition system. CHA and CHB are the input channels and EXT is the external trigger channel of the DAQ card.

3.4.2 Image Reconstruction

To achieve a good balance between the lateral resolution and computation time, 2D SAFT was applied separately along two orthogonal directions rather than applying 3D SAFT directly [11, 49-51]. As shown in Figs. 11(a) and (b), the cone-shaped 3D imaging space were decomposed into 60 concentric circular planes and 128 sector planes, which are perpendicular to each other. For each circular plane, a B-Scan image was reconstructed from the 256 A-lines (with 8192 pixels in each) with and without applying SAFT, respectively. For each sector planes, a B-scan image was reconstructed from the 120 A-lines (with 8192 pixels in each) with and without applying SAFT, respectively. Next, the B-Scan images for the 60 circular planes and the 128 sector planes were

normalized and combined together pixel by pixel to reconstruct the 3D image reconstruction, which consists of a total number of $60 \times 256 \times 8192$ voxels. The voxels were further regrouped onto 8192 C-Scan images in Cartesian coordinates and saved into the png format (Fig. 3.11(c)). At last, the 8192 C-Scan images were stacked together to create a 3D view in Volview (Kitware) (Fig. 3.3.11 (d)).

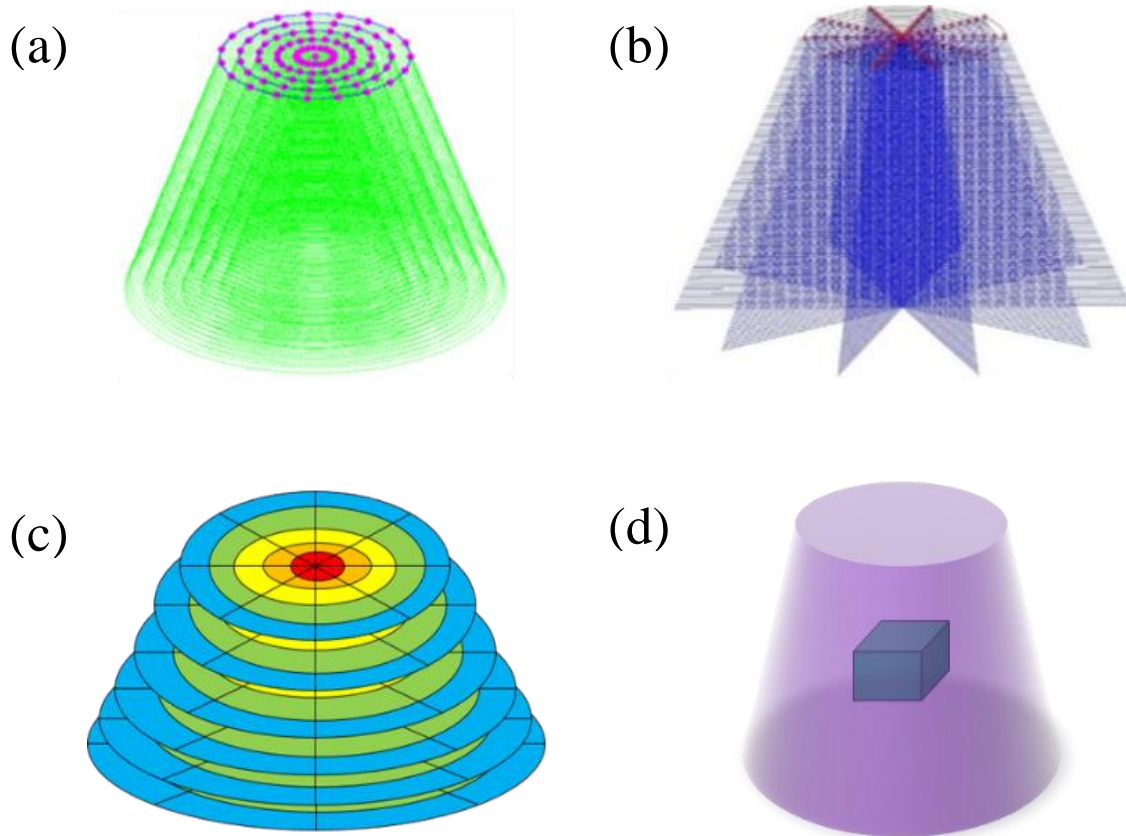


Figure 3.11 3D Image reconstruction process. (a) Circular B-Scan image reconstruction. (b) Sector B-Scan image reconstruction. (c) C-Scan image slicing. (d) 3D image formation.

Applying 2D SAFT on the circular and sector planes is similar with that on Cartesian coordinates, except that the observation distance between a detection point and a reconstruction pixel needs to be calculated in a different way. As shown in Fig. 3.12(a), for applying SAFT on a circular plane, the observation distance (ρ) from an ultrasound detection point (T_i) to a reconstruction pixel (P_j) can be calculated as

$$\rho = \sqrt{c^2 + d^2} \quad (3.3)$$

$$c = \sqrt{r^2 + r'^2 - 2rr' \cos \varphi} \quad (3.4)$$

$$d = \delta \cos \theta \quad (3.5)$$

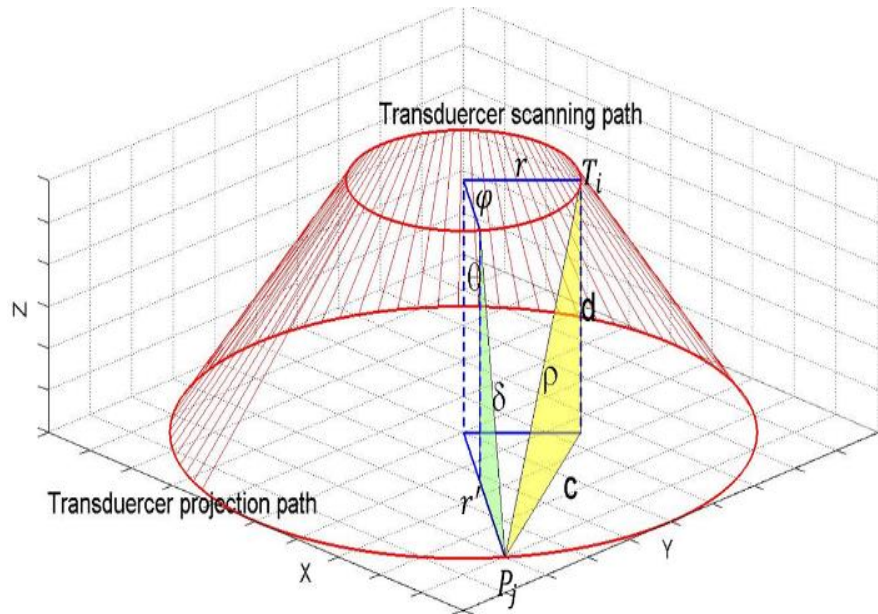
where d is the distance between the two c-planes bounding T_i and P_j , respectively, r is the diameter of the circular path passing the detection point (T_i), r' is the diameter of the circular path passing the reconstruction pixel (P_j), θ is the scanning angle of the transducer, and φ is the angle between the two sector planes bounding T_i and P_j , respectively. For applying SAFT on a sector plane (Fig. 3.12(b)), the observation distance can be calculated as

$$\rho = \sqrt{l^2 + l'^2 - 2ll' \cos \Delta\theta} \quad (3.6)$$

where l is the distance from the ultrasound detection point (T_i) to the anchor point of the hinge, l' is the distance from the reconstruction pixel (P_j) to the anchor point of the hinge, and $\Delta\theta$ is the cross angle between T_i and P_j with respect to the anchor point. The mapped pixel of each A-Line signal can be determined by summarizing the values of signal strength (after Hilbert transformation) based on the

corresponding acoustic delay times determined by dividing the observation distance by the acoustic velocity.

(a)



(b)

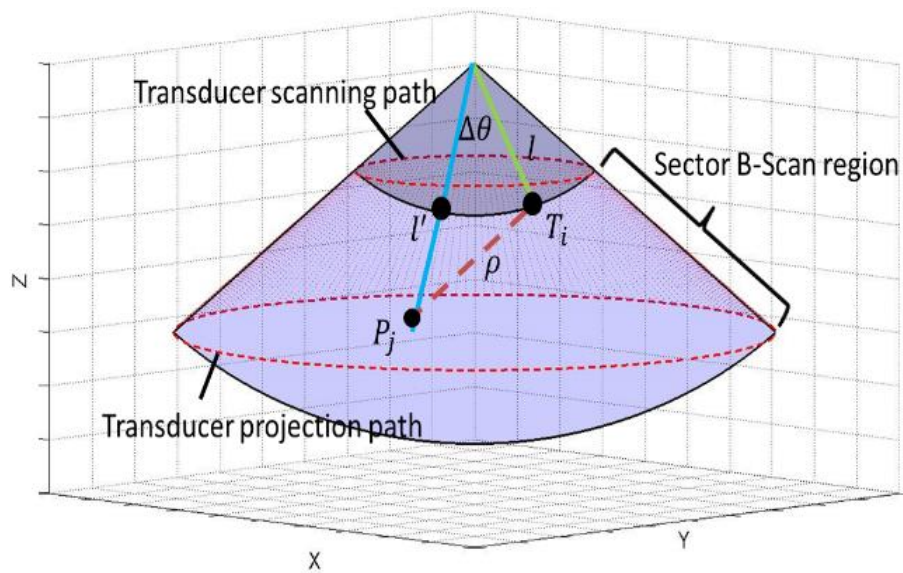


Figure 3.12 Illustration of the geometry for the calculation of the observation distance for SAFT. (a) on circular planes. (b) on sector planes..

3.5 Imaging Experiments and Results

Fig. 3.13 shows the imaging target for the ultrasound imaging experiments with the scanning transducer. It consists of two silicon discs with a diameter of 6 mm, which are supported with four optical fibers with a diameter of 100 μm . To fix the optical fibers in place, four acrylic plates with an array of positioning holes were made by laser cutting and assembled together with epoxy. The distances between the two silicon discs are 15 mm, 10 mm, and 20 mm, respectively. Due to their small diameter, the back-scattered ultrasound signals from the optical fibers will be weak and therefore would not interfere with those from the two silicon discs. During the ultrasound imaging experiment, the entire assembly was placed underneath the scanning transducer setup and completely immersed in water.

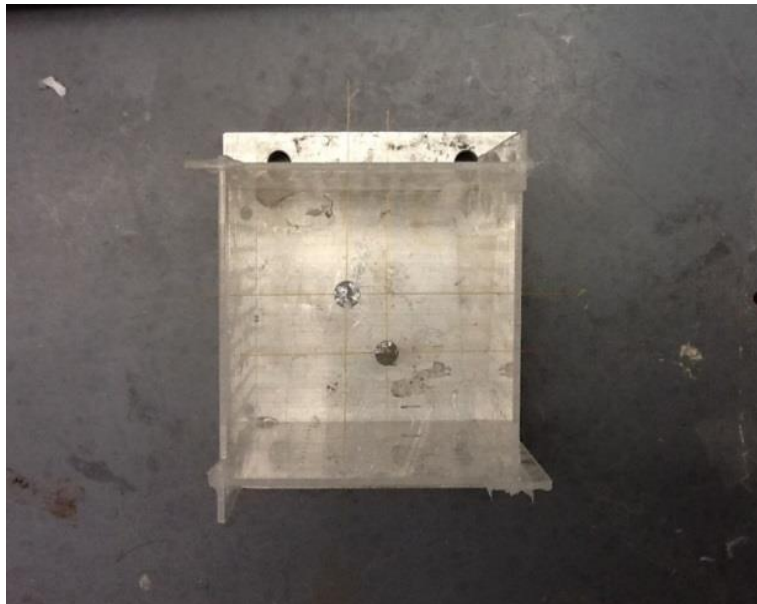


Figure 3.13 Picture of the imaging target.

3.5.1 Alignment of the Detection Points

To implement the 2D SAFT on both circular and sector planes, the ultrasound detection points need to be positioned on the 2D grid formed by the circular and sector planes. However, due to the random time delay (ϵ) between the trigger signals from the LabView controlled computer and the driving signals from the function generators, the ultrasound detection points on the circular scanning paths could be misaligned (Fig. 3.14(a)). In addition, when the scanning of the transducer is shift from one circular path to another, some ultrasound detection points could appear on the transition section between two circular paths. To address this issue, the data recording of the DAQ card was delayed by a time (τ) (longer than ϵ) to exclude those off-path detection points. The recording period (σ) was still equal to the period of the driving signal. The relative location of an ultrasound detection point on a circular scanning path is determined by the time and therefore the phase of the AC driving signals (see Fig. 3.8). Therefore, the ultrasound detections points on the circular scanning paths can be re-aligned based on the phase of the corresponding driving signals. (Fig. 3.14(b))

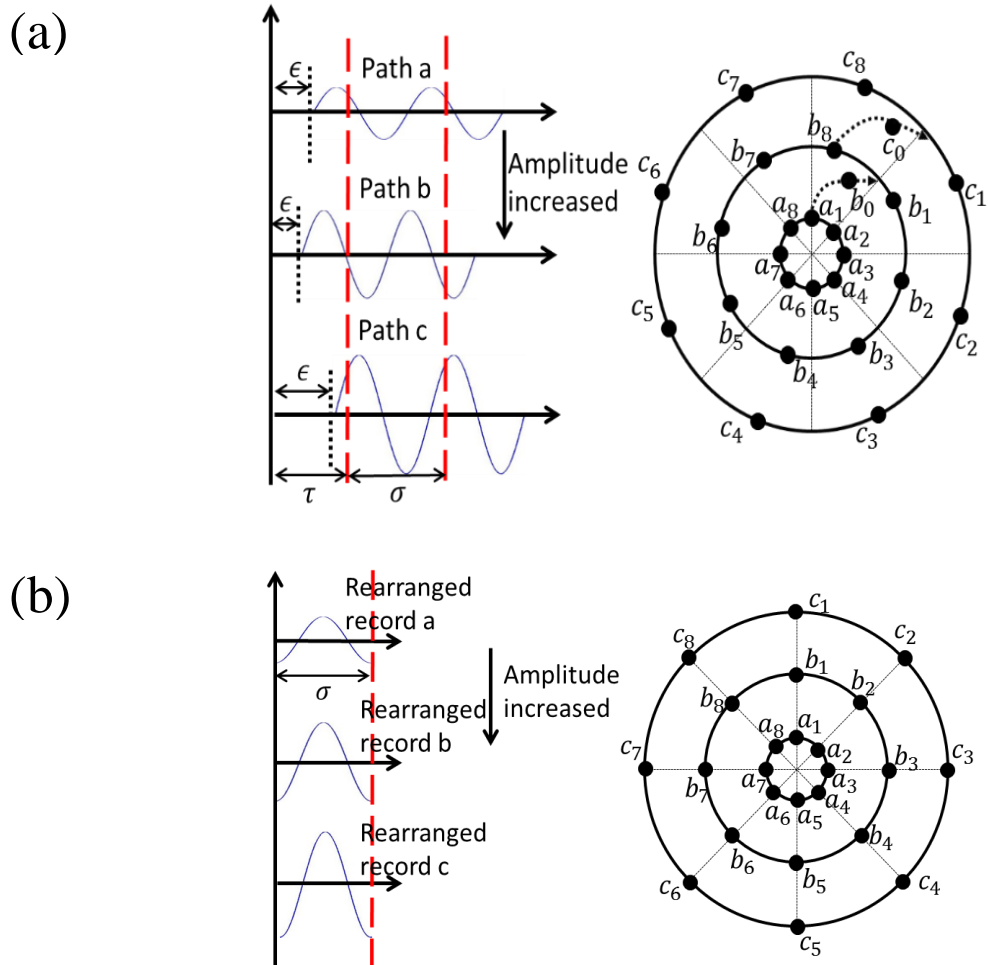
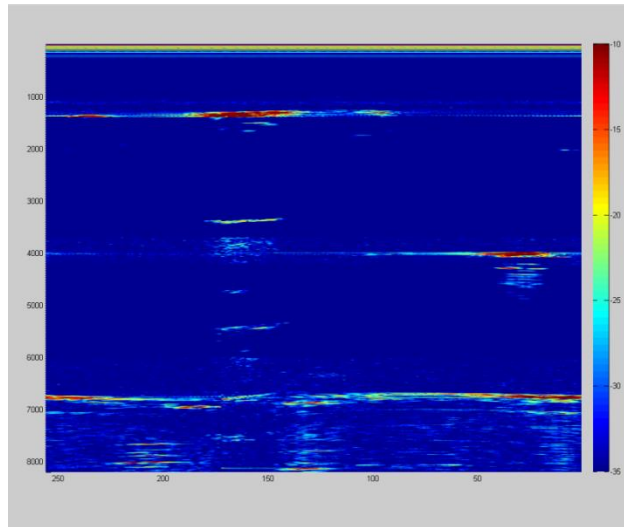


Figure 3.14 (a) Random time delay in the AC driving signals and the resulting misalignment of the ultrasound detection points. (b) Re-alignment of the ultrasound detection points based on the AC driving signals.

3.5.2 *Image Reconstruction*

Fig. 3.15(a) shows the raw B-Scan image (before applying SAFT) of a representative circular plane reconstructed from the 256 A-line data. Fig. 3.15(b) shows the B-Scan image of the same circular plane after applying SAFT. The reverberation signals from the ultrasound echo traveled back and forth between sample and transducer were canceled by using the reverberation nulling and echo prediction method [52-54]. The signals reflected from the aluminum plate at the bottom of acrylic holder and from the tip of transducer itself were also removed. A similar image processing procedure was adopted for the section plane. Fig. 3.15(c) and 3.15(d) show the B-Scan images of one representative sector plane before and after applying SAFT. Both images consist of 120 A-line data.

(a)



(b)

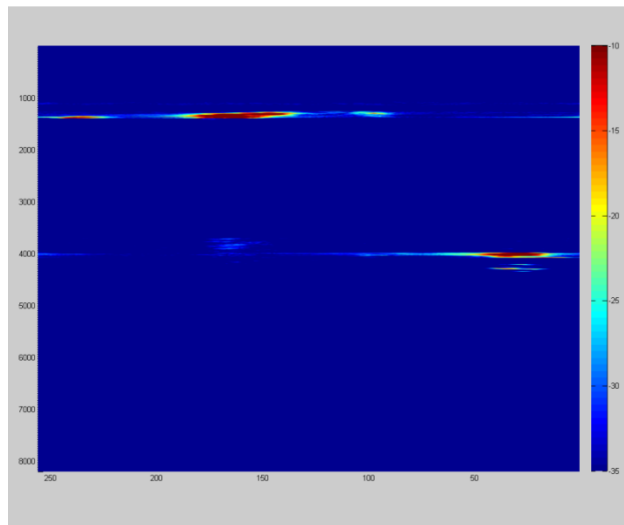
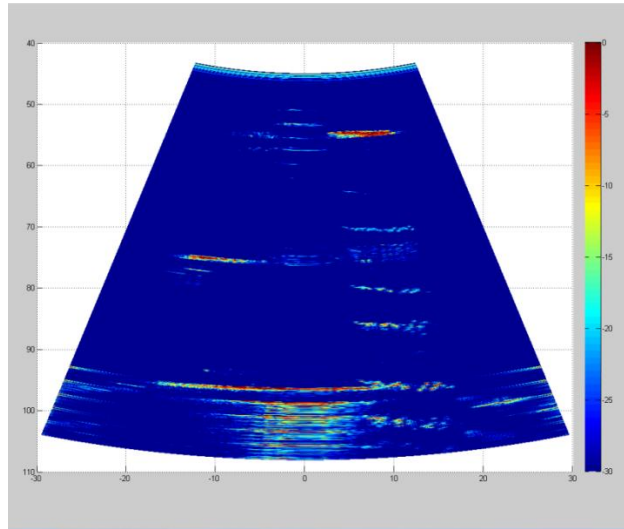


Figure 3.15 B-Scan image of a representative circular plane (a) before and (b) after applying SAFT. B-Scan image of a representative sector plane (c) before and (d) after applying SAFT.

(c)



(d)

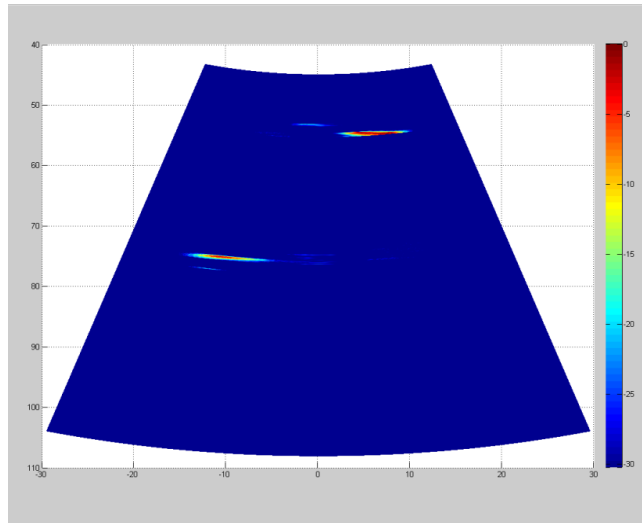


Figure 3.15 Continued.

Fig. 3.16(a) shows the reconstructed 3D image based on the raw B-Scan images of both the circular and sector planes. The C-Scan images with gradually increased diameters can be clearly seen. The margin of the graphs excluding the Cartesian coordinates is presented in white color. In order to provide a better view of the two imaging targets, most of the margin was removed by using the shrink function in

Volview (Fig. 3.16(b)). However, in order to keep the image of the two targets intact, a small portion of the white margin at the upper-left corner has to be kept and therefore is also shown in the plot. Fig. 3.16(c) shows the reconstructed 3D image based on the B-Scan images of both the circular and sector planes after applying SAFT. Compared with the image without SAFT, both the contrast and spatial resolution of the imaging targets were significantly improved. The mean diameters of the upper and lower silicon discs were estimated to be 6.28 mm and 5.83 mm, respectively, which close to the actual dimension (6 mm). The distances between the two silicon pieces along x, y, and z axes were estimated to be 14.2 mm, 9.88 mm, and 20.11 mm, respectively, which match well with their actual values.

(a)

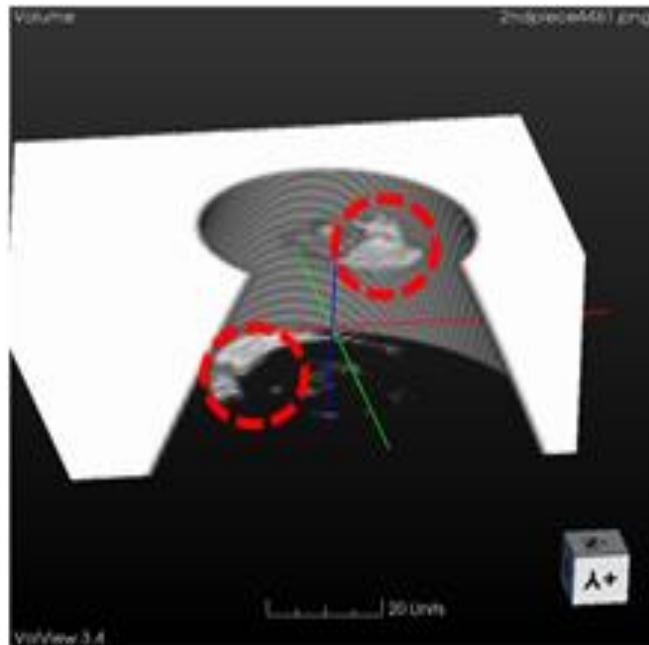
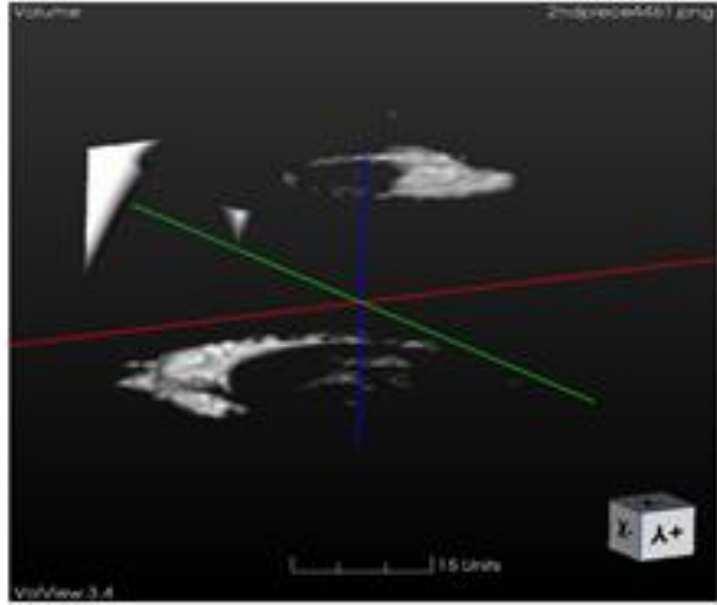


Figure 3.16 Reconstructed 3D ultrasound images in Volview. (a) Raw image. (b) Image with white margin removed. (c) Image with white margin removed and after applying SAFT. The red, green and blue lines indicate the x y and z axes.

(b)



(c)

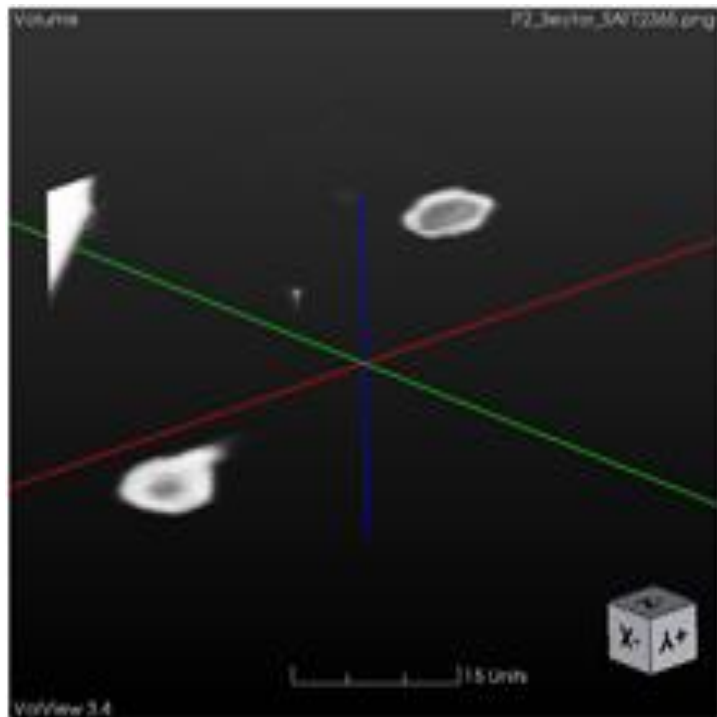


Figure 3.16 Continued.

4. MULTI-LAYER TRANSDUCER ARRAY FOR ACOUSTIC TOMOGRAPHY

4.1 Introduction

Ultrasound transducer array (1D or 2D) is an essential part for ultrasound 3D image which is useful non-destructive diagnostic technique with a wide range of applications [8, 55, 56]. To achieve 3D ultrasound imaging, acoustic signals have to be recorded from 2D positions. At present, most of the 3D ultrasound imaging is achieved by ultrasound transducer array which can be used to generate and receive ultrasound signals from 2D elements either independently or by group [14, 17, 57, 58]. Through using 2D transducer array to conduct “electronic” acoustic scan in a curvature 2D plane by manipulating the phase or delay time of ultrasonic pulse generators and recording the echo signals respectively [13, 18, 19, 22]. 3D imaging could be reconstructed through the acoustic scanning path and delay time between transmitted and reflected ultrasonic signals. Nevertheless, to record echo signals or generate acoustic pulses through a large number (100s~10000s) of transducer elements, complex electronics including multiplexer, pulser/receiver, and data acquisition (DAQ) system are required which make the entire imaging system could become complex, bulky, power-consuming, and expensive [12, 16, 38, 59]. As a result, these techniques are mainly good for on-site diagnose or research use and are not suitable for economical handheld operations. Therefore, a novel 2D transducer array is necessary for many applications which need barely enough resolution or imaging high contrast targets where SNR is supposed to be good, but have requirements for mobile ability, imaging speed, and cost-effective.

In this research, a novel strategy of building 2D ultrasound transducer array with PVDF which enable high speed and low cost 3D ultrasound imaging was reported. The 2D ultrasound transducer array was consisted by two 1D transducer arrays manufactured by patterning metal layer of PVDF sheets. When acoustic signals arrive PVDF film, the compression and relax motion will generate voltage difference between upper and bottom conductive layers. By reading the voltage values of each section individually, each 1D array could be used to build a B-Scan image. The ultrasound signals from these two 1D arrays of locations will be stacked together to reconstruct a 3D image. The number of transducer elements could be reduced from the multiplication of two 1D arrays to the summation of them. The amount of ultrasound pulse generator, channels of high speed DAQ card, control elements, and multiplexers could be dramatically decreased. The 2D PVDF transducer array can be further miniature and patterned with transparent conductive layers to allow optical signals penetrate from it. Therefore, it could provide a new approach for high speed, compact, and low-cost 3D ultrasound and photoacoustic imaging systems.

4.2 Device Concept and Feasibility Study

4.2.1 Device Concept

The concept of using two 1D arrays to collect 2D information for 3D imaging reconstruction could be simplified as using two 1D optical detection elements to build a 2D image. Assume there are two laser spots with center aligned horizontally and same light density were imaged by two transparent, completely overlapped, and perpendicular

1D photo sensor arrays. (Fig. 4.1(a)) For 1D array with vertical alignment elements the imaging result should be two rectangles where the intensity would be proportional to the illuminated area like Fig. 4.1(b) shows. Similarly, the horizontal aligned 1D array will be a horizontal stripe. (Fig. 4.1(c)) Through stacking these results together, the positions and dimensions of two objects could be retrieved with partially shape distortion. (Fig. 4.1(d))

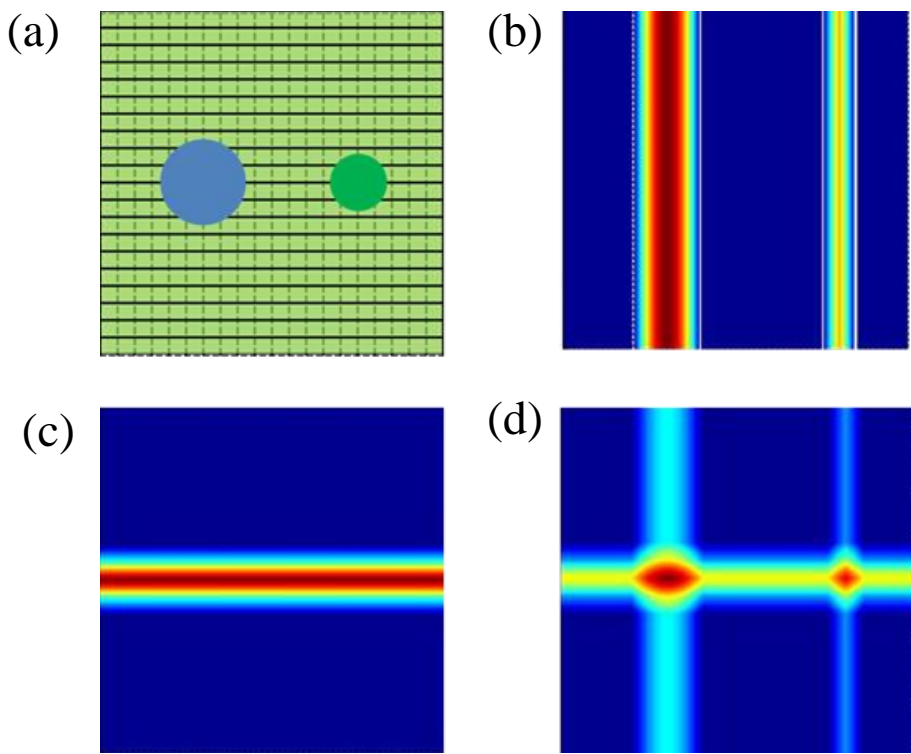


Figure 4.1 2D Image reconstruction process. (a) Schematic of laser spot on top of two transducer arrays (line: 1D array at the top, dot: 1D array at the bottom.) (b) Imaging results of horizontal 1D array. (c) Imaging results of vertical 1D array. (d) Reconstructed 2D image.

4.2.2 Feasibility Study

A preliminary imaging experiment was conducted to evaluate the feasibility of the concept discussed above through comparing the 3D imaging results of 16x16 elements ultrasound array and 16 elements plus 16 elements multi-layer array. The system setup was shown in Fig. 4.2, a 1Hz pulsed signal generated by function generator was used to synchronize the motion of linear translation stages and the ultrasound pulse of pulser/receiver. The echo signals received by pulser/receiver will be recorded by DAQ card. A single element ultrasound transducer with 10MHz resonance frequency and 2mm diameter was immersed in a water tank. The water tank was carried by two stacked linear translation stages which allows it to move along both x and y directions. The total imaging region was $32 \times 32 \text{mm}^2$ and the step size was 2mm (Fig. 4.2). The total numbers of recorded pulse/echo signals would be 256. The imaging sample was consisted by two 6mm diameter with 100um thickness silicon discs. The top view of imaging sample was showed as Fig. 4.2(a) the distances between two discs were 15 mm along x axis, 10 mm along y axis, and 10 mm depth difference.

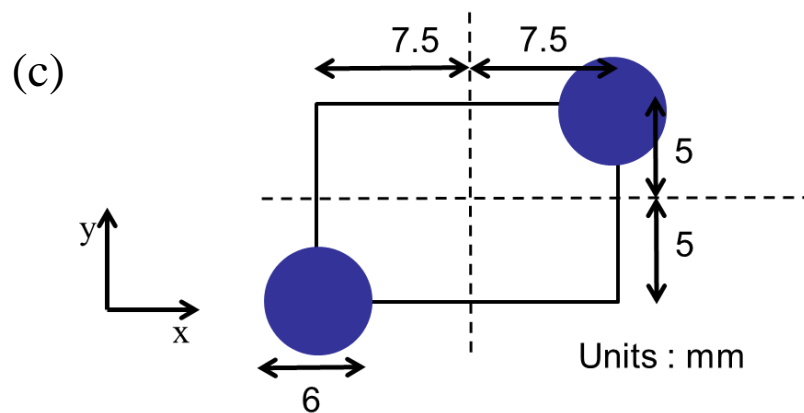
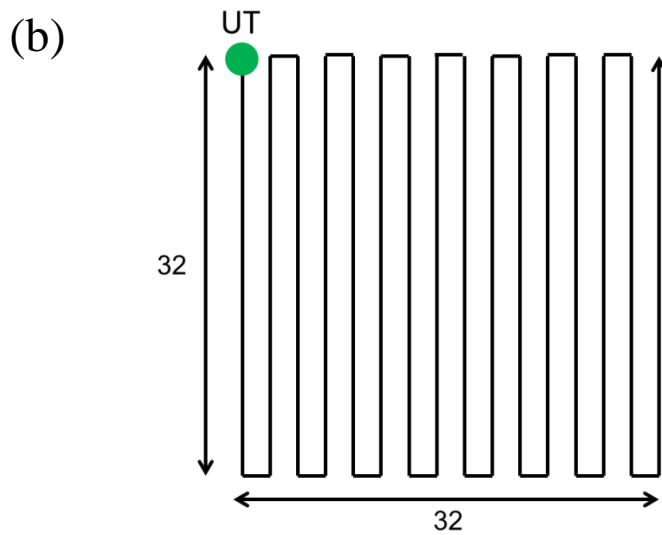
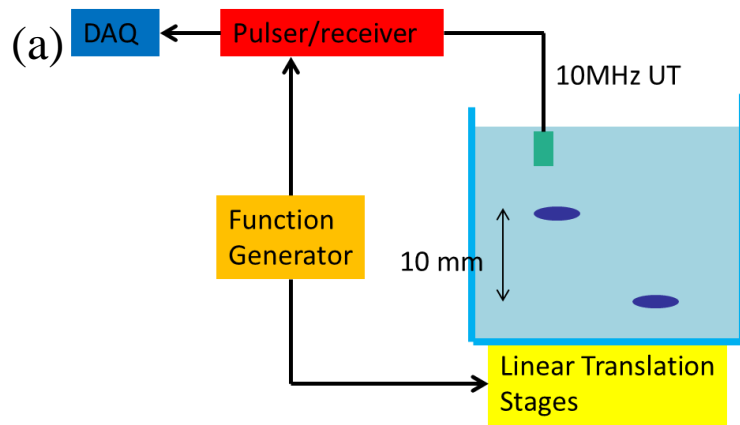


Figure 4.2 (a) System setup of feasibility study experiment. (b) Traveling path of single element transducer. (c) Top view of imaging sample.

Fig. 4.3(a) shows the raw 3D imaging result of using A-Scan signals from 16x16 different locations. Through averaging the results of 16 elements into one channel along x and y directions respectively, two 16 channel 2D images was generated. By using the stacking 1D array imaging reconstruction process, a raw 3D imaging reconstruction result with the same dynamic range as last result was showed by Fig. 4.3(b). The resolution of using 16 plus 16 channels methodology was relatively low especially for the deeper target. However, the positions of two discs were clearly the same and the resolution can be improved by simply using different dynamic range. With this imaging result, the concept of using multiple layers of 1D transducer array to replace 2D transducer array should be consider as feasible. By using this technique, it is obviously the channel numbers of DAQ card and transducer elements can be reduced from 256 to 32 without sacrificing the imaging speed.

(a)

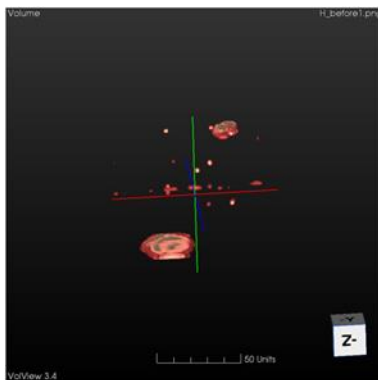


Figure 4.3 (a) 3D imaging result of signals from 16x16 locations. (b) 3D imaging result of signals from 16 plus 16 rectangular locations.

(b)

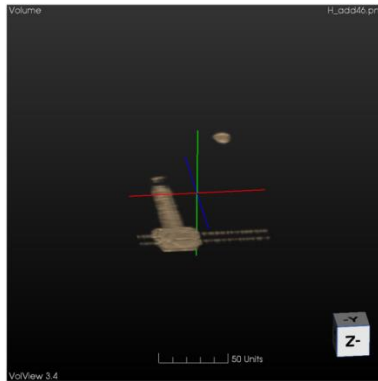


Figure 4.3 Continued

4.3 Design, Construction and Characterization

4.3.1 Design and Construction

Theoretically, ultrasound waves will introduce charges when it contact with PVDF film and cause the vibration on it due to piezoelectric phenomenon. These electrical signals could be detected and transmitted if there are conductive layers covered on each side of PVDF film. Therefore, certain portion of PVDF film coated with metals could serve as an acoustic detect element. Moreover, if there are multiple regions of PVDF film patterned by conductive materials isolated. These covered islands could serve as multiple ultrasound detection elements. Besides, the array elements most close to the bombard area should have strongest voltage difference which could use to determine the locations of acoustic signals. Although PVDF could also be used to generate ultrasound signals through applying voltage on each side, it is a much better ultrasound receiver rather than transmitter [55, 60-64]. In this research, it is mainly severed as receiver while doing ultrasound transmission mode imaging.

To enable 3D ultrasound imaging, 2D A-Scan information from both x and y direction are necessary. As Fig. 4.4(a) (b) indicates, 16 copper stripes are patterned on PVDF film where grounding Ni/Cu layer are coated on another side. The overlap regions of Ni/Cu strips and common grounding layer could serve as 16 different ultrasound transducer elements. Two PVDF films are bonded together like Fig. 4.4(c) shows, where array elements from two rectangular 1D array were aligned perpendicularly.

Fig. 4.4(d) shows the constructed prototype of the 2D PVDF ultrasound transducer array. Two 64mmx64mm PVDF film with 110um thickness and coated with 8um Ni/Cu on both side (3-1003702-7, Measurement Specialties, Inc.) was used to build the transducer array. Photolithography process was used to pattern transducer elements by using photoresist as mask with chemical etching. As Fig 4.4(a) indicates, the transducer area was consisted by sixteen 1.53125mmx32mm rectangular strips with 0.5mm intervals. Besides, sixteen 3mmx3mm pads with 1mm interval and connections between transducer elements and pads were also patterned on the same side. Fig. 4.4(b) shows the layout of another side which include 32mmx32mm ground area and 3mmx10mm ground pad with conducting copper layer. Two transducer array were than bonded together by using conductive epoxy (ESOLDER30222OZ, Von Roll) like Fig. 4.4(c) indicates. Since water is the most common medium of ultrasound imaging applications, the entire 2D transducer array was coated with Teflon as hydrophobic layer and sealed inside a case made by acrylic with laser cutting to ensure the waterproof ability. (Fig. 4.4(d))

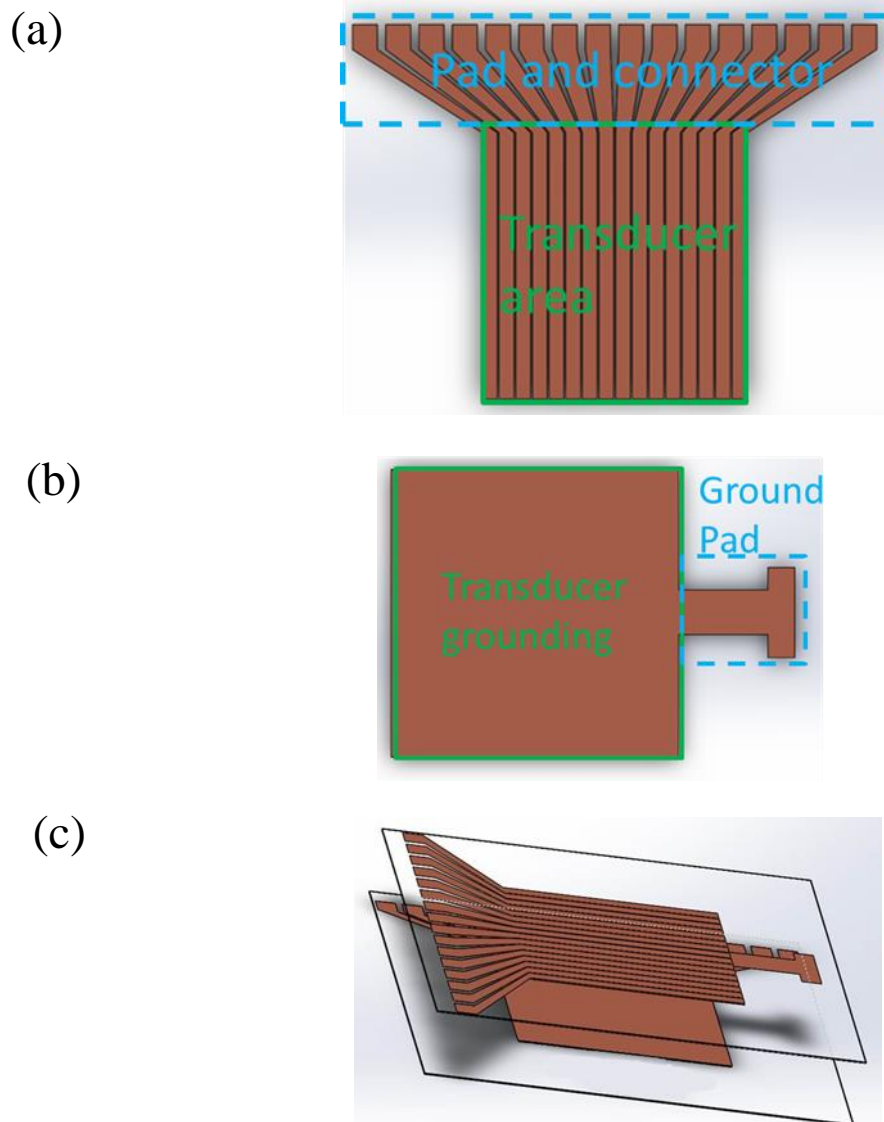


Figure 4.4 (a) Schematic of the transducer array and pads design. (b) Schematic of the common ground side and its pad. (c) Illustration of two 1D transducer arrays bonded together. (d) Picture of 2D PVDF transducer array.

(d)

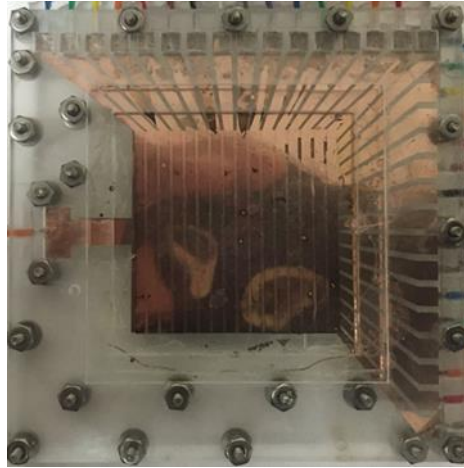


Figure 4.4 Continued.

The resonant frequency of ultrasonic transducer made by piezoelectric materials and works on thickness mode can be calculated by equation 4.1. Where thickness t defines the resonance frequency f of the device given by with the first harmonic resonant frequency being $n = 1$, where n is an odd integer, and c_p is the acoustic wave velocity in the piezoelectric material. In this research, two 110 μ m PVDF films were stacked and the acoustic velocity of PVDF is 2250m/s which turns out the resonant frequency of our 2D PVDF transducer array will be about 5.11 MHz.

$$f = n \frac{c_p}{2t} \quad (4.1)$$

4.3.2 Characterization

To characterize the frequency response of PVDF film, a simple PVDF stacked transducer was used to receive photoacoustic signals generate from rubber tape, hex wrench, and lead. A 2.25 MHz transducer (V106-RM, Olympus NDT) was used to

receive the ultrasound signals from targets at the same time as comparison. A Q-switched Nd:YAG laser system was used to deliver laser pulses with a wavelength of 532 nm and a duration of 8 ns. (Fig. 4.5(a)) Because of thermal expansion effect, the targets will generate acoustic signals after heated by such a short pulse duration laser. The illumination area is 10mm× 10mm and the optical energy density was $\sim 20 \text{ mJ/cm}^2$. A pulser-receiver (5072PR, Olympus) synchronized with pulse laser was used to amplify ultrasound signals. As Fig 4.5(b) (c) (d) indicates, the center frequency of upper layer, bottom layer and stacked PVDF film transducer are between 4 MHz to 5 MHz because the conductive epoxy and metal layers could slightly increase the thickness. The frequency domain of two single layers and stacked layer were similar which shows the bonding process successfully merge two PDVF films together. The photoacoustic signals received by 2.25 MHz transducer were mostly below 2 MHz since the attenuation of ultrasound signals was proportional to the frequency and the distance between transducer and targets were much larger than PVDF films and targets.

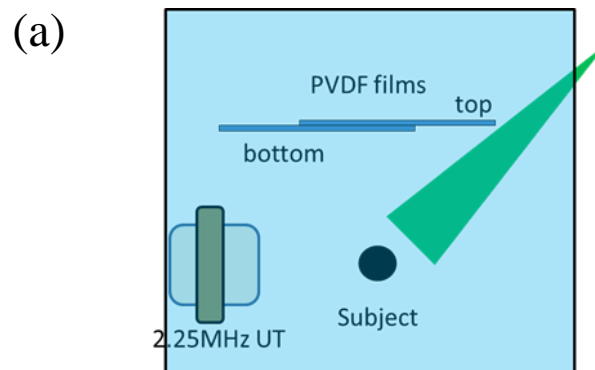
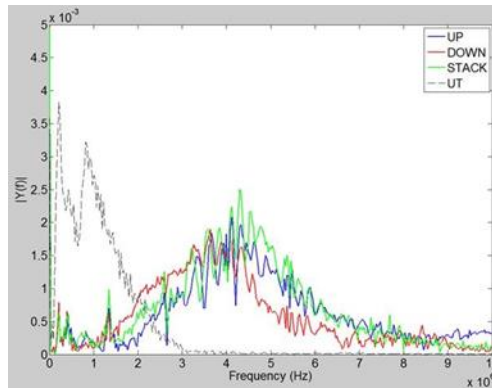
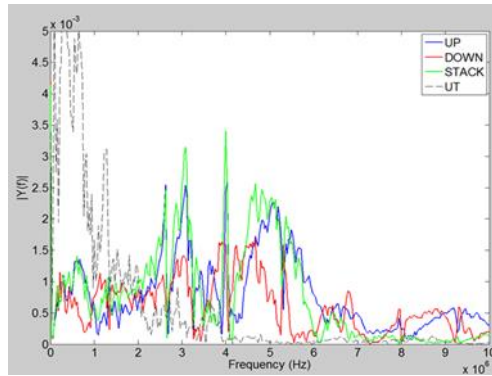


Figure 4.5 Setup of frequency characterization experiment (a) and the results for different targets including (b) rubber tape, (c) hex wrench, and (d) pencil lead.

(b)



(c)



(d)

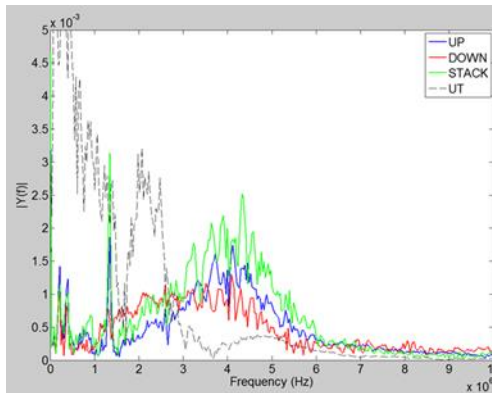


Figure 4.5 Continued.

To characterize the sensitivity of each PVDF transducer element, a single element ultrasound transducer (XMS-310-B, Olympus) with center frequency of 10 MHz, 6-dB bandwidth of 80%, and diameter of 2 mm was used to scan the 1D

transducer array. During each scanning process, only one element from 1D transducer array was active to record the acoustic signals generate by single element transducer. The scanning step is 2mm on both directions and the result will represented with summation voltage signals after Hilbert transform during certain time interval. Fig. 4.6 shows the results of scanning 16 times for each layer, each pixel represented the integrated amplitude in certain time interval. As predicted, in most of the graphs, the strongest amplitude received by PVDF transducer elements happened when the single element transducer traveled right on top of the activated element. Some graphs, the intensity distribution is not perfectly matched with active area. It is due to the PVDF film itself will transmit vibrations and generate charges on activated elements even the ultrasound source is not on top of it. Besides, the electrical conductivity of each element might be nonuniform after photolithography process.

(a)

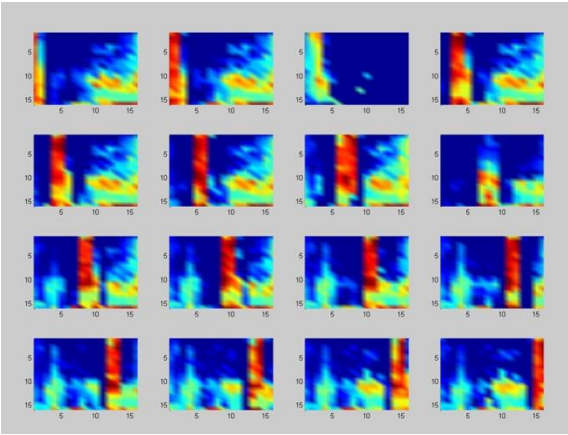


Figure 4.6 Results of ultrasound sensitivity experiment of (a) top layer and (b) bottom layer.

(b)

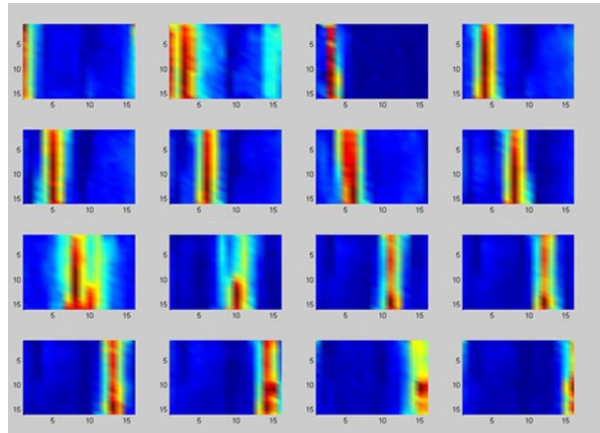


Figure 4.6 Continued.

4.4 Data Acquisition and Image Reconstruction

4.4.1 Data Acquisition

A schematic of the data acquisition system is shown in Fig. 4.7(a). The pulser-receiver (5072PR, Olympus) was set to external trigger mode with amplification of 50 dB and damping ratio of 20 ohm. A personal computer with LabView (version 2013, National Instruments) installed was used to switch the ultrasound elements through multiplexer IC arrays (74HC4052, NXP Semiconductor) and trigger the pulser/receiver by using DAQ card A (PCI6251, National Instrument). The ultrasound signal will maintain its time domain characteristics where the amplitude would be slightly attenuated after going through multiplexers. (Fig. 4.7(b)) The amplified ultrasound signals were recorded by DAQ card B (AT9350-128M, Alazar Technologies) after being triggered by the DAQ card A. The data collection of DAQ card B was setup with 250 MHz sampling rate and 8192 sampling points. After the data from all the 16 1D elements on the top layer were

recorded 20 times, the active transducer array switched manually by connecting the cable of multiplexer array to the transducer arrays on the bottom. In the end, a total of $20 \times 32 \times 8192$ sampling points for the ultrasound signals were acquired and saved on the computer for image reconstruction.

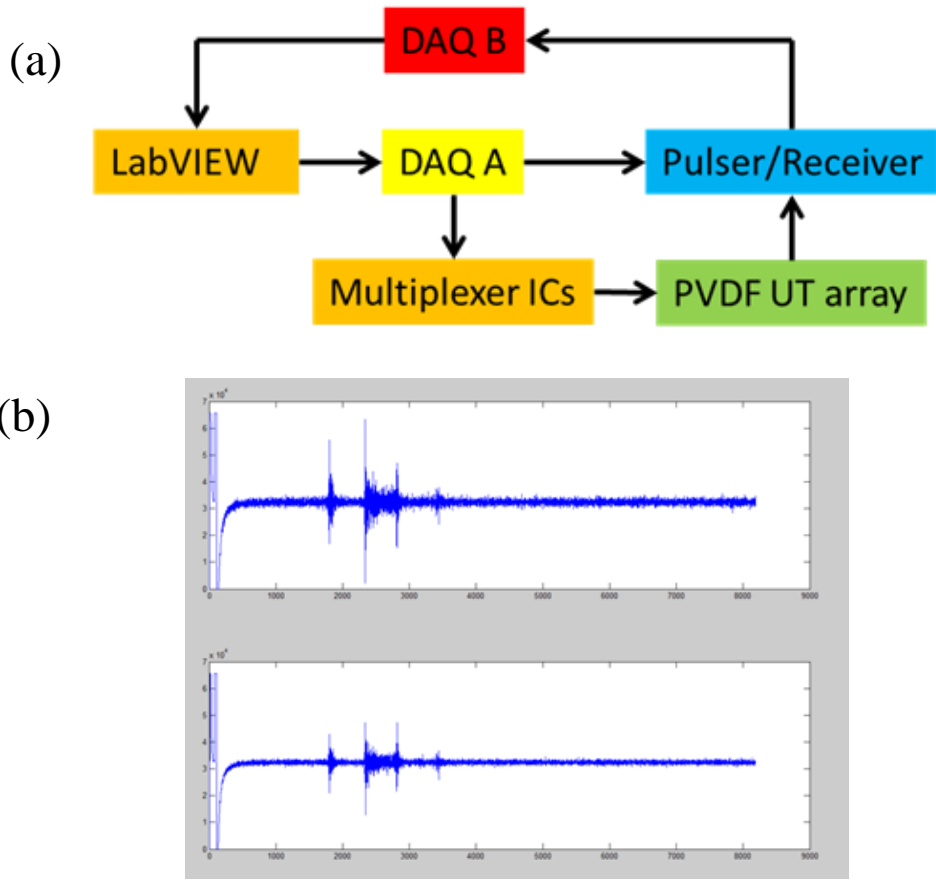


Figure 4.7 (a) Schematic of the data acquisition system. (b) Received ultrasound signals before (Top) and after (Bottom) multiplexer IC.

4.4.2 *Image Reconstruction*

The imaging reconstruction process of PVDF multi-layer transducer array could be demonstrated by using two sets of 16 A-Scan signals. The A-Scan results are set from two perpendicular ultrasound arrays. Assume a target was put under the 12th rectangular element of 1D array aligned along x direction and 4th rectangular element of 1D ultrasound array aligned along y direction. It is possible to simulate the A-Scan results using MATLAB like Fig. 4.8 (a) (b) indicates. After Hilbert transform, both B-Scan results is shown by Fig. 4.8(c) where the graph on the top indicates the B-Scan image of x direction array and the graph on the bottom represents the B-Scan image of y direction array. For reconstructing 3D image with these two B-Scan results, B-Scan imaging from x direction alignment transducer elements have to be extended along y direction to form a 3D volumetric image like top graph of Fig. 4.8(d) shows. The same process is applied to y direction transducer array and the result is shown on the bottom of Fig. 4.8(d). Through summarize the amplitude pixel by pixel of these two 3D images and tuning the dynamic range, 3D imaging reconstructed from two 1D ultrasound transducer arrays could be achieved as Fig. 4.8(e) indicates.

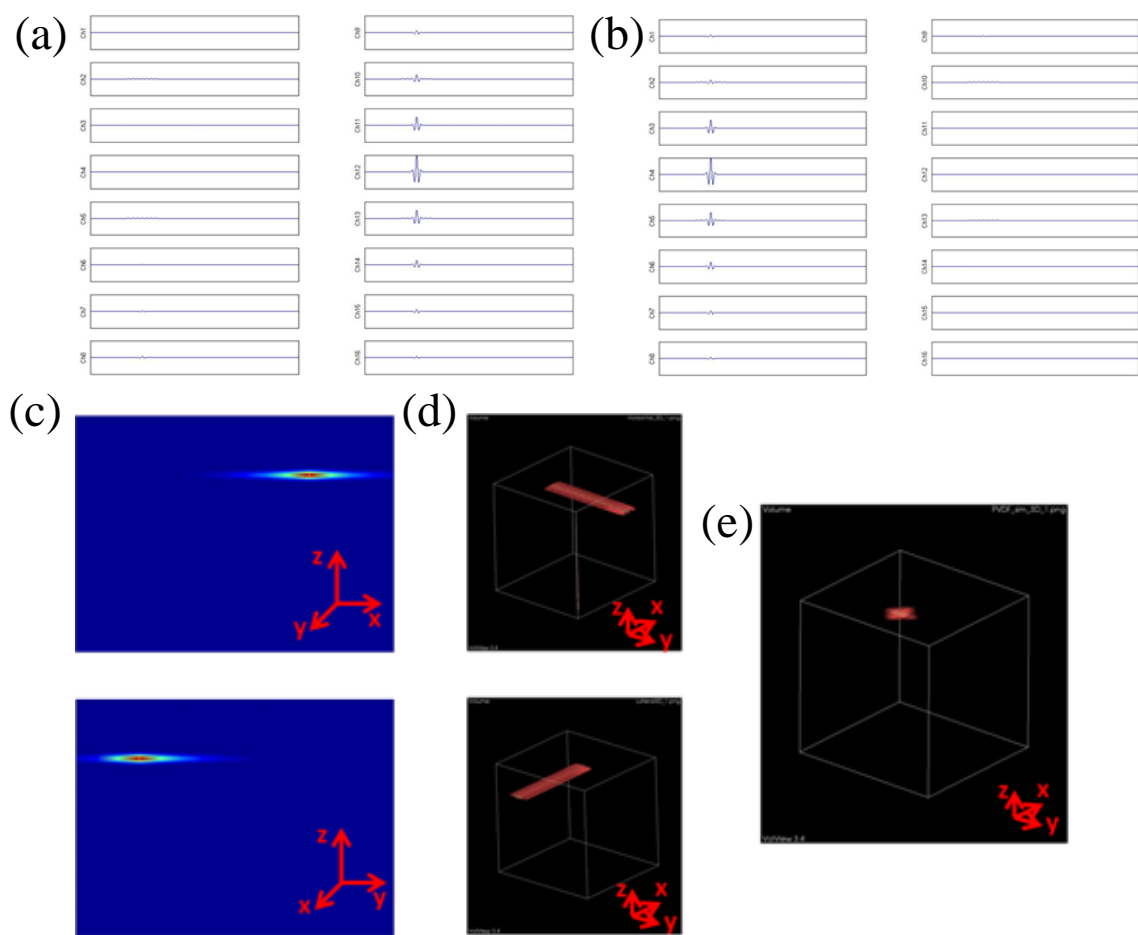


Figure 4.8 Simulation of (a) A-Scan results from 16 channels ultrasound transducer array which aligned along x direction. (b) A-Scan results from 16 channels ultrasound transducer array which aligned along y direction. (c) B-Scan result of x direction ultrasound array (Top) and y direction ultrasound array (Bottom). (d) 3D B-Scan image of direction ultrasound array (Top) and y direction ultrasound array (Bottom). (e) Result of 3D imaging reconstruction.

4.5 Imaging Experiment and Results

Fig. 4.9(a) (b) shows the design of imaging setup and the imaging targets for the ultrasound transmission mode imaging experiments with PVDF 2D ultrasound transducer array. The target was consisted by two 4mmx10mm rectangular silicon pieces, which were supported by two 100um diameter optical fibers. To fix the optical fibers in

place, two acrylic plates with an array of positioning holes were made by laser cutting and assembled together with silicone. The distances between the two silicon pieces are 15mm in z direction and 1mm along x direction, respectively. Due to their small diameter, the back-scattered ultrasound signals from the optical fibers will be weak and therefore would not interfere with those from the two silicon pieces. During the ultrasound imaging experiment, the entire assembly was placed underneath the PVDF 2D ultrasound transducer array and completely immersed in water.

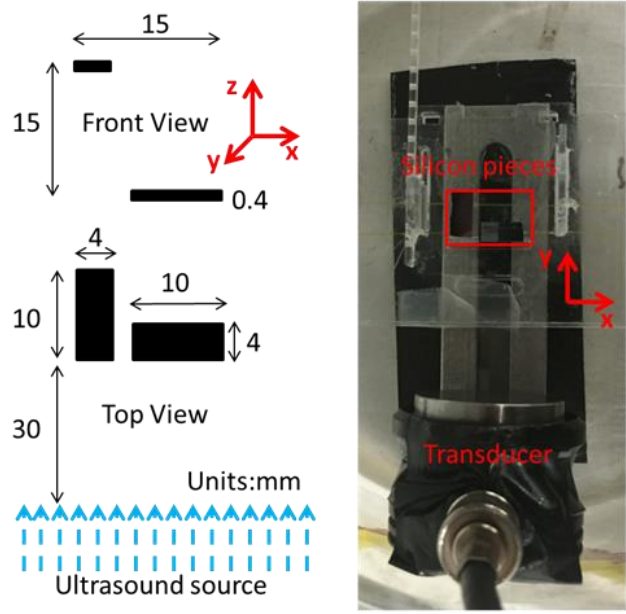


Figure 4.9 (a) Alignment of imaging targets and (b) Picture of the imaging target.

4.5.1 Experimental Setup

Fig. 4.10 shows the system setup of 3D imaging reconstruction experiment. The data recording process was mentioned above; a 2.25 MHz single element transducer (V105-RM, Olympus NDT) with 19mm diameter nominal element size was selected to be ultrasound source with 30mm away from the silicon pieces. Its large diameter could provide uniform acoustic signals for ultrasound transmission mode imaging experiment like Fig. 4.9(a) showed. In the bottom layer of 2D PVDF transducer array was 1D transducer array aligned along x direction where 1D transducer array aligned along y direction was on the top layer. The repetition rate of DAQ card A was set to 200 Hz and the total data acquisition time for each layer was 1.6s.

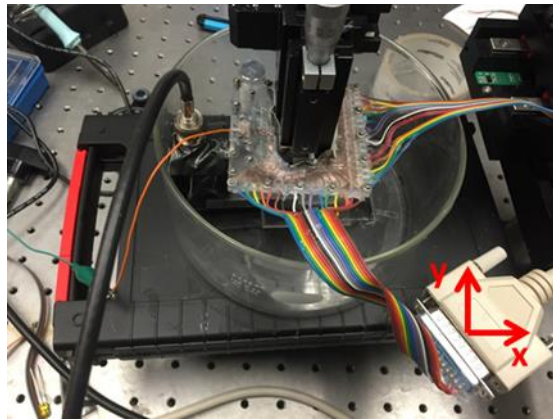


Figure 4.10 Picture of 3D imaging reconstruction experiment.

4.5.2 Imaging Results

To reconstruct B-Scan image, first, 20 A-Scan results of each channel will be averaged to eliminate white noise. After that, Hilbert transform was applied to transfer

voltage signals into amplitudes of acoustic energy. Fig. 4.11(a) indicates the imaging result of top layer elements which aligned along y direction. In Fig. 4.11(a), the upper object was 12mm wide and the lower one is 6mm. The result from bottom layer elements was shown in Fig. 4.11(b) where the top object is 4mm wide and lower object is 12mm wide. The dimensions were not totally agreement with the real values since the acoustic signals diverged radially after going out form silicon pieces which make the imaging results blur especially for the lower object. Besides, the elements size would limit the resolution of raw B-Scan image. As mentioned before, in order to reconstruct 3D image from these two B-Scan results, both graphs has to extrude along x or y directions. After it, these two 3D images will be added together pixel by pixel. The result of 3D imaging reconstruction was shown in Fig. 4.11(c); the positions of two objects were close to real situation where the shape was distorted especially for the lower silicon piece.

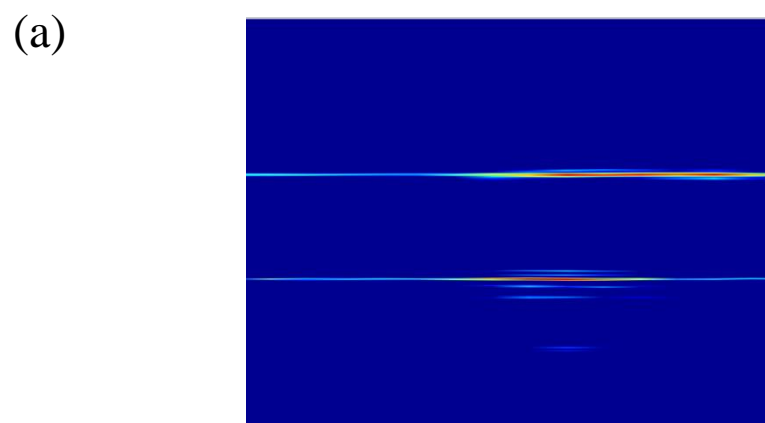
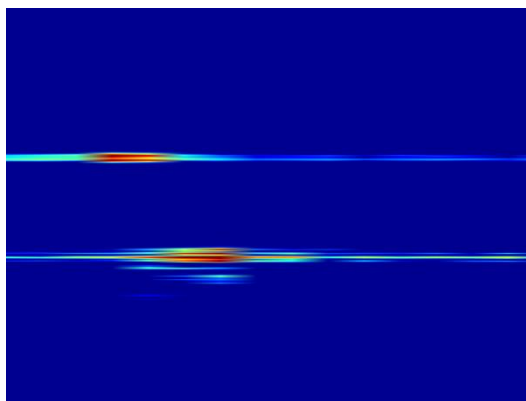


Figure 4.11 B-Scan image of 1D transducer arrays (a) top layer (b) bottom layer and (c) the result of 3D imaging reconstruction.

(b)



(c)

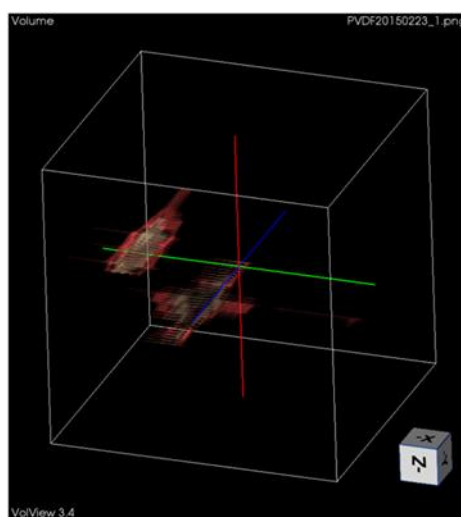


Figure 4.11 Continued.

5. CONCLUSIONS AND FUTURE WORK

In this dissertation, three micromachined scanning devices have been studied for different 3D acoustic imaging applications. Specifically, the water-immersible scanning mirror microsystem is useful for acoustic microscopy to scan focused ultrasound beams. The micromechanical scanning transducer is useful for high-resolution portable 3D imaging, where high-density transducer array with small element size were often required. The multi-layer transducer array is useful for high-speed 3D imaging, where all the ultrasound data need to be collected within a single transmitting-receiving cycle.

First, a two-axis scanning mirror microsystem is demonstrated, which is specially designed for reliable and fast underwater scanning of both optical and ultrasonic beams. The liquid-immersible electromagnetic microactuator provided fast and energy-efficient 2-axis mechanical scanning. This made the acquisition of all the ultrasound data for 3D image reconstruction to be performed in a timely manner. This unique feature can be potentially used to enhance the imaging capability of scanning acoustic microscopy and photoacoustic microscopy where a liquid matching medium is needed. Future work will focus on the optimization and further miniaturization of the scanning mirror microsystem and also its application in new ultrasound and photoacoustic microscopic imaging modalities.

Second, a two-axis micromechanical scanning transducer technique was developed and 3D pulse-echo ultrasound imaging of two silicon discs immersed in water as the imaging target was successfully conducted. The lateral resolution of the 3D ultrasound image was improved with modified SAFT algorithms based on the unique

format of the acquired ultrasound data. The scanning transducer technique doesn't involve complex and expensive data acquisition (DAQ) electronics, which are otherwise required in the ultrasound-array based imaging systems. Ultrasound imaging at different frequency ranges can be easily obtained by using a single-element transducer with suitable frequency response. This work laid a foundation for the development of compact and low-cost hand-held scanning transducer probes for 3D ultrasound imaging. In the future, feedback control will be developed to improve the stability of the mechanical scanning. New functionalities (e.g., optical delivery) will be investigated to expand the imaging capability (e.g., photoacoustic tomography) of the scanning transducer probe.

Last, a prototype of multi-layer ultrasound transducer array for low-cost and high-speed 3D imaging system has been demonstrated. It could provide a new economical solution for high-speed 3D ultrasound imaging. In the future, the design and fabrication of the multi-layer transducer array will be further improved to increase the detection sensitivity and reduce inter-element cross-talk. In addition, new data acquisition electronics will be developed to provide better interface with the multi-layer transducer array.

REFERENCES

- [1] S. W. Smith, H. G. Pavy, and O. T. Vonramm, "High-Speed Ultrasound Volumetric Imaging-System .1. Transducer Design and Beam Steering," *Ieee Transactions on Ultrasonics Ferroelectrics and Frequency Control*, vol. 38, pp. 100-108, Mar 1991.
- [2] A. Fenster and D. B. Downey, "Three-dimensional ultrasound imaging," *Annu Rev Biomed Eng*, vol. 2, pp. 457-75, 2000.
- [3] A. Fenster and D. B. Downey, "3-D ultrasound imaging: A review," *Ieee Engineering in Medicine and Biology Magazine*, vol. 15, pp. 41-51, Nov-Dec 1996.
- [4] G. R. Lockwood, J. R. Talman, and S. S. Brunke, "Real-time 3-D ultrasound imaging using sparse synthetic aperture beamforming," *Ieee Transactions on Ultrasonics Ferroelectrics and Frequency Control*, vol. 45, pp. 980-988, Jul 1998.
- [5] R. W. Prager, R. N. Rohling, A. H. Gee, and L. Berman, "Rapid calibration for 3-D freehand ultrasound," *Ultrasound Med Biol*, vol. 24, pp. 855-69, Jul 1998.
- [6] R. N. Rohling, A. H. Gee, and L. Berman, "Automatic registration of 3-D ultrasound images," *Ultrasound Med Biol*, vol. 24, pp. 841-54, Jul 1998.
- [7] X. Ye, J. A. Noble, and D. Atkinson, "3-D freehand echocardiography for automatic left ventricle reconstruction and analysis based on multiple acoustic windows," *IEEE Trans Med Imaging*, vol. 21, pp. 1051-8, Sep 2002.
- [8] J. P. S. Garcia, P. T. Garcia, R. B. Rosen, and P. T. Finger, "A 3-dimensional ultrasound C-scan imaging technique for optic nerve measurements," *Ophthalmology*, vol. 111, pp. 1238-1243, Jun 2004.
- [9] Q. H. Huang, Y. P. Zheng, R. Li, and M. H. Lu, "3-D measurement of body tissues based on ultrasound images with 3-D spatial information," *Ultrasound in Medicine and Biology*, vol. 31, pp. 1607-1615, Dec 2005.
- [10] V. Grau, H. Becher, and J. A. Noble, "Registration of multiview real-time 3-D echocardiographic sequences," *IEEE Trans Med Imaging*, vol. 26, pp. 1154-65, Sep 2007.
- [11] R. Jirik, I. Peterlik, N. Ruiter, J. Fousek, R. Dapp, M. Zapf, *et al.*, "Sound-Speed Image Reconstruction in Sparse-Aperture 3-D Ultrasound Transmission

- Tomography," *Ieee Transactions on Ultrasonics Ferroelectrics and Frequency Control*, vol. 59, pp. 254-264, Feb 2012.
- [12] D. H. Turnbull and F. S. Foster, "Fabrication and Characterization of Transducer Elements in 2-Dimensional Arrays for Medical Ultrasound Imaging," *Ieee Transactions on Ultrasonics Ferroelectrics and Frequency Control*, vol. 39, pp. 464-475, Jul 1992.
- [13] J. M. Bureau, W. Steichen, and G. Lebail, "A two-dimensional transducer array for real-time 3D medical ultrasound imaging," *1998 Ieee Ultrasonics Symposium - Proceedings, Vols 1 and 2*, pp. 1065-1068, 1998.
- [14] E. D. Light, R. E. Davidsen, J. O. Fiering, T. A. Hruschka, and S. W. Smith, "Progress in two-dimensional arrays for real-time volumetric imaging," *Ultrason Imaging*, vol. 20, pp. 1-15, Jan 1998.
- [15] A. A. Oraevsky, V. G. Andreev, A. A. Karabutov, and R. O. Esenaliev, "Two-dimensional opto-acoustic tomography transducer array and image reconstruction algorithm," *Laser-Tissue Interaction X: Photochemical, Photothermal, and Photomechanical, Proceedings Of*, vol. 3601, pp. 256-267, 1999.
- [16] G. Rizzatto, "Evolution of ultrasound transducers: 1.5 and 2D arrays," *Eur Radiol*, vol. 9 Suppl 3, pp. S304-6, 1999.
- [17] O. Oralkan, A. S. Ergun, C. H. Cheng, J. A. Johnson, M. Karaman, T. H. Lee, *et al.*, "Volumetric ultrasound Imaging using 2-D CMUT arrays," *Ieee Transactions on Ultrasonics Ferroelectrics and Frequency Control*, vol. 50, pp. 1581-1594, Nov 2003.
- [18] E. D. Light and S. W. Smith, "Combined 2D array transducers/deployment kits for real-time 3D ultrasound guidance of interventional devices," *2007 Ieee Ultrasonics Symposium Proceedings, Vols 1-6*, pp. 844-847, 2007.
- [19] Y. P. Jia, M. L. Xu, M. Y. Ding, and M. Yuchi, "3D ultrasound coherence imaging based on 2D array design," *Medical Imaging 2013: Ultrasonic Imaging, Tomography, and Therapy*, vol. 8675, 2013.
- [20] A. Dhanantwari, S. Stergiopoulos, C. Parodi, F. Bertora, P. Pellegretti, and A. Questa, "Adaptive 3D beamforming for ultrasound systems deploying linear and planar phased array probes," *2003 Ieee Ultrasonics Symposium Proceedings, Vols 1 and 2*, pp. 1855-1858, 2003.

- [21] R. Held, T. N. Nguyen, and S. Vaezy, "Transvaginal 3D image-guided high intensity focused ultrasound array," *4th International Symposium on Therapeutic Ultrasound*, vol. 754, pp. 170-173, 2005.
- [22] M. F. Rasmussen and J. A. Jensen, "3D ultrasound imaging performance of a row-column addressed 2D array transducer: a simulation study," *Medical Imaging 2013: Ultrasonic Imaging, Tomography, and Therapy*, vol. 8675, 2013.
- [23] S. W. Smith, P. Gardea, V. Patel, S. J. Douglas, and P. D. Wolf, "Double Ring Array Catheter for In Vivo Real-Time 3D Ultrasound," *Ultrasonic Imaging*, vol. 36, pp. 167-176, Jul 2014.
- [24] P. M. Hagelin, U. Krishnamoorthy, J. P. Heritage, and O. Solgaard, "Scalable optical cross-connect switch using micromachined mirrors," *Ieee Photonics Technology Letters*, vol. 12, pp. 882-884, Jul 2000.
- [25] V. X. D. Yang, Y. X. Mao, B. A. Standish, N. R. Munce, S. Chiu, D. Burnes, *et al.*, "Doppler optical coherence tomography with a micro-electro-mechanical membrane mirror for high-speed dynamic focus tracking," *Optics Letters*, vol. 31, pp. 1262-1264, May 1 2006.
- [26] H. Ra, W. Piyawattanametha, Y. Taguchi, D. Lee, M. J. Mandella, and O. Solgaard, "Two-dimensional MEMS scanner for dual-axes confocal microscopy," *Journal of Microelectromechanical Systems*, vol. 16, pp. 969-976, Aug 2007.
- [27] W. Y. Jung, S. Tang, D. T. McCormic, T. Q. Xie, Y. C. Ahn, J. P. Su, *et al.*, "Miniaturized probe based on a microelectromechanical system mirror for multiphoton microscopy," *Optics Letters*, vol. 33, pp. 1324-1326, Jun 15 2008.
- [28] C. Liu, *Foundations of MEMS*. Upper Saddle River, NJ: Pearson Prentice Hall, 2006.
- [29] W. H. Chen, E. J. Gottlieb, J. M. Cannata, Y. F. Chen, and K. K. Shung, "Development of sector scanning ultrasonic backscatter microscope," *2000 Ieee Ultrasonics Symposium Proceedings, Vols 1 and 2*, pp. 1681-1684, 2000.
- [30] L. V. Wang, "Multiscale photoacoustic microscopy and computed tomography," *Nature Photonics*, vol. 3, pp. 503-509, Sep 2009.
- [31] J. Xia, Z. J. Guo, K. Maslov, A. Aguirre, Q. Zhu, C. Percival, *et al.*, "Three-dimensional photoacoustic tomography based on the focal-line concept," *Journal of Biomedical Optics*, vol. 16, Sep 2011.

- [32] J. J. Yao, K. I. Maslov, Y. Zhang, Y. N. Xia, and L. V. Wang, "Label-free oxygen-metabolic photoacoustic microscopy in vivo," *Journal of Biomedical Optics*, vol. 16, Jul 2011.
- [33] J. J. Yao and L. H. V. Wang, "Photoacoustic tomography: fundamentals, advances and prospects," *Contrast Media & Molecular Imaging*, vol. 6, pp. 332-345, Sep-Oct 2011.
- [34] C. A. Van Eysden and J. E. Sader, "Resonant frequencies of a rectangular cantilever beam immersed in a fluid," *Journal of Applied Physics*, vol. 100, Dec 1 2006.
- [35] P. I. Greguss, *Ultrasonic imaging : seeing by sound : the principles and widespread applications of image formation by sonic, ultrasonic, and other mechanical waves*, 1st ed. London ; New York: Focal Press, 1980.
- [36] T. L. Szabo, *Diagnostic ultrasound imaging : inside out*. Amsterdam ; Boston: Elsevier Academic Press, 2004.
- [37] Q. H. Huang, Y. P. Zheng, M. H. Lu, and Z. R. Chi, "Development of a portable 3D ultrasound imaging system for musculoskeletal tissues," *Ultrasonics*, vol. 43, pp. 153-163, Jan 2005.
- [38] I. O. Wygant, X. Zhuang, D. T. Yeh, O. Oralkan, A. Sanli Ergun, M. Karaman, *et al.*, "Integration of 2D CMUT arrays with front-end electronics for volumetric ultrasound imaging," *IEEE Trans Ultrason Ferroelectr Freq Control*, vol. 55, pp. 327-42, Feb 2008.
- [39] F. Forsberg, "Ultrasonic biomedical technology; marketing versus clinical reality," *Ultrasonics*, vol. 42, pp. 17-27, Apr 2004.
- [40] R. G. Maev, *Advances in acoustic microscopy and high resolution imaging*. Weinheim Chichester: Wiley-VCH ;John Wiley distributor, 2013.
- [41] A. S. Savoia, G. Caliano, and M. Pappalardo, "A CMUT Probe for Medical Ultrasonography: From Microfabrication to System Integration," *Ieee Transactions on Ultrasonics Ferroelectrics and Frequency Control*, vol. 59, pp. 1127-1138, Jun 2012.
- [42] C. M. Lee, C. J. Engelbrecht, T. D. Soper, F. Helmchen, and E. J. Seibel, "Scanning fiber endoscopy with highly flexible, 1 mm catheterscopes for wide-field, full-color imaging," *J Biophotonics*, vol. 3, pp. 385-407, Jun 2010.

- [43] M. T. Myaing, D. J. MacDonald, and X. D. Li, "Fiber-optic scanning two-photon fluorescence endoscope," *Optics Letters*, vol. 31, pp. 1076-1078, Apr 15 2006.
- [44] G. J. Tearney, S. A. Boppart, B. E. Bouma, M. E. Brezinski, N. J. Weissman, J. F. Southern, *et al.*, "Scanning single-mode fiber optic catheter-endoscope for optical coherence tomography," *Opt Lett*, vol. 21, pp. 543-5, Apr 1 1996.
- [45] E. S. Barhoum, R. S. Johnston, and E. J. Seibel, "Optical modeling of an ultrathin scanning fiber endoscope, a preliminary study of confocal versus non-confocal detection," *Optics Express*, vol. 13, pp. 7548-7562, Sep 19 2005.
- [46] E. J. Seibel and Q. Y. J. Smithwick, "Unique features of optical scanning, single fiber endoscopy," *Lasers in Surgery and Medicine*, vol. 30, pp. 177-183, 2002.
- [47] E. J. Seibel, Q. Y. J. Smithwick, C. M. Brown, and P. G. Reinhall, "Single fiber flexible endoscope: general design for small size, high resolution, and wide field of view.," *Biomonitoring and Endoscopy Technologies*, vol. 1, pp. 29-39, 2001.
- [48] C. H. Huang, J. J. Yao, L. H. V. Wang, and J. Zou, "A water-immersible 2-axis scanning mirror microsystem for ultrasound and photoacoustic microscopic imaging applications," *Microsystem Technologies-Micro-and Nanosystems-Information Storage and Processing Systems*, vol. 19, pp. 577-582, Apr 2013.
- [49] Z. L. Deng, X. Q. Yang, H. Gong, and Q. M. Luo, "Two-dimensional synthetic-aperture focusing technique in photoacoustic microscopy," *Journal of Applied Physics*, vol. 109, May 15 2011.
- [50] C. H. Frazier and W. D. O'Brien, "Synthetic aperture techniques with a virtual source element," *Ieee Transactions on Ultrasonics Ferroelectrics and Frequency Control*, vol. 45, pp. 196-207, Jan 1998.
- [51] N. V. Ruitter, G. F. Schwarzenberg, M. Zapf, and H. Gemmeke, "Conclusions from an Experimental 3D Ultrasound Computer Tomograph," *2008 Ieee Nuclear Science Symposium and Medical Imaging Conference (2008 Nss/Mic), Vols 1-9*, pp. 3776-3783, 2009.
- [52] T. Folegot, C. Prada, and M. Fink, "Resolution enhancement and separation of reverberation from target echo with the time reversal operator decomposition," *Journal of the Acoustical Society of America*, vol. 113, pp. 3155-3160, Jun 2003.
- [53] S. G. Parulekar, "Ultrasonic-Detection of Calcification in Gallstones - the Reverberation Shadow," *Journal of Ultrasound in Medicine*, vol. 3, pp. 123-129, 1984.

- [54] H. C. Song, W. S. Hodgkiss, W. A. Kuperman, K. G. Sabra, T. Akal, and M. Stevenson, "Passive reverberation nulling for target enhancement," *Journal of the Acoustical Society of America*, vol. 122, pp. 3296-3303, Dec 2007.
- [55] F. S. Foster, E. A. Harasiewicz, and M. D. Sherar, "A history of medical and biological imaging with polyvinylidene fluoride (PVDF) transducers," *Ieee Transactions on Ultrasonics Ferroelectrics and Frequency Control*, vol. 47, pp. 1363-1371, Nov 2000.
- [56] C.-H. Huang, J. Yao, L. V. Wang, and J. Zou, "A water-immersible 2-axis scanning mirror microsystem for ultrasound and photoacoustic microscopic imaging applications," *Microsystem technologies*, vol. 19, pp. 577-582, 2013.
- [57] R. A. Kruger, W. L. Kiser, D. R. Reinecke, and G. A. Kruger, "Thermoacoustic computed tomography using a conventional linear transducer array," *Medical Physics*, vol. 30, pp. 856-860, May 2003.
- [58] W. B. Qiu, Y. Y. Yu, H. R. Chabok, C. Liu, F. K. Tsang, Q. F. Zhou, *et al.*, "A Flexible Annular-Array Imaging Platform for Micro-Ultrasound," *Ieee Transactions on Ultrasonics Ferroelectrics and Frequency Control*, vol. 60, pp. 178-186, Jan 2013.
- [59] X. D. Wang, J. Cannata, D. DeBusschere, C. H. Hu, J. B. Fowlkes, and P. Carson, "A High-Speed Photoacoustic Tomography System based on a Commercial Ultrasound and a Custom Transducer Array," *Photons Plus Ultrasound: Imaging and Sensing 2010*, vol. 7564, 2010.
- [60] M. A. O'Reilly and K. Hynynen, "A PVDF Receiver for Ultrasound Monitoring of Transcranial Focused Ultrasound Therapy," *Ieee Transactions on Biomedical Engineering*, vol. 57, pp. 2286-2294, Sep 2010.
- [61] G. R. Harris, R. C. Preston, and A. S. DeReggi, "The impact of piezoelectric PVDF on medical ultrasound exposure measurements, standards, and regulations," *Ieee Transactions on Ultrasonics Ferroelectrics and Frequency Control*, vol. 47, pp. 1321-1335, Nov 2000.
- [62] Q. Zhang, P. A. Lewin, and P. E. Bloomfield, "Variable frequency multilayer PVDF transducers for ultrasound imaging," *Ultrasonic Transducer Engineering*, vol. 3037, pp. 2-12, 1997.
- [63] Q. F. Zhou, S. T. Lau, D. W. Wu, and K. Shung, "Piezoelectric films for high frequency ultrasonic transducers in biomedical applications," *Progress in Materials Science*, vol. 56, pp. 139-174, Feb 2011.

- [64] J. Liu and R. Shandas, "Optimizing the Design of a 2D Array Piezoelectric Micromachined Ultrasound Transducer for 3D Echo Particle Image Velocimetry," *2006 Ieee Ultrasonics Symposium, Vols 1-5, Proceedings*, pp. 2329-2332, 2006.

APPENDIX

MATLAB AND LABVIEW PROGRAMS

In this dissertation most of the imaging reconstruction and processing were done by MATLAB. The algorithms of imaging processing and reconstructions had been mentioned above, where the programs of how to implement circular SAFT, sector SAFT, and generating 2D images for 3D reconstruction with MATLAB were also attached.

In this dissertation, all the data acquisition process were controlled by LabVIEW. LabVIEW is a graphic language which makes it easier to learning and programing. Here the control program of high speed DAQ card (ATS9350, Alazar tech) was attached. It basically modified the source code from our vendor.

```

%Sector SAFT
%I: original image
%A: [1 4 9 ... 78^2]*1.419E-4^2 depth
a=1:12000;
A=a.^2*(0.77E-2)^2; %units:mm, depth look up table
%theta=-0.3120:0.0184:0.3120;
s=0; %register of target position amplitude
%Sector_SAFT_1=zeros(8001,33,210);

for k=151:210
%P32SAFT=P32(:, :, k);
I=SR_all_n0(2000:10000, :, k);
background=mean(I(:, 1));
Sector_SAFT_1(:, :, k)=background;
m=10; % neighboring rows
for x=1:1:33 % target lateral position
    for y=3000:1:5000 % target depth

        for i=round(max(1, x-m)):1:round(min(33, x+m)) % total
Vitual Ultrasound sources
            a=(y+1050)*0.77E-2+62;
            b=62;
            d=a^2+b^2-2*a*b*cos(abs(x-i)*0.0195); % 2000-950=1050,
cos theory, a^2+b^2-2*abcos(theta)=d^2
            [c, j]=min(abs(sqrt(A)-sqrt(d)));

            if c>0.001
                s=s+background;
            elseif i>28||i<5
                s=s+background;
            else
                s=s+I(j-2000, i);
            end

        end

        if round(x+m)>33
            %P32SAFT(y, x, k)=s/round((x/4+m-32)); % numbers of
source siganls being added when x+m>32
            Sector_SAFT_1(y, x, k)=s/(round(min(33, x+m))-
round(max(1, x-m))+1);
        elseif round(x-m)<1
            %P32SAFT(y, x, k)=s/round((m-x/4+1)); % numbers of
source siganls being added when x-m<1
            Sector_SAFT_1(y, x, k)=s/(round(min(33, x+m))-
round(max(1, x-m))+1);

        else
            Sector_SAFT_1(y, x, k)=s/(round(min(33, x+m))-
round(max(1, x-m))+1);
        end
    end
end

```

```

                                s=0;
        end
    end
    m=5;
    for x=1:1:33
        for y=5500:1:7500                % target depth

            for i=round(max(1,x-m)):1:round(min(33,x+m))    % total
                Vitural Ultrasound sources
                a=(y+1050)*0.77E-2+62;
                b=62;
                d=a^2+b^2-2*a*b*cos(abs(x-i)*0.0195);        % 2000-950=1050,
                cos theory, a^2+b^2-2*abc*cos(theta)=d^2
                [c,j]=min(abs(sqrt(A)-sqrt(d)));

                if c>0.001
                    s=s+background;
                else
                    s=s+I(j-2000,i);
                end
            end

            if round(x+m)>33
                %P32SAFT(y,x,k)=s/round((x/4+m-32));        % numbers of
                source siganls being added when x+m>32
                Sector_SAFT_1(y,x,k)=s/(round(min(33,x+m))-
                round(max(1,x-m))+1);
            elseif round(x-m)<1
                %P32SAFT(y,x,k)=s/round((m-x/4+1));        % numbers of
                source siganls being added when x-m<1
                Sector_SAFT_1(y,x,k)=s/(round(min(33,x+m))-
                round(max(1,x-m))+1);
            else
                Sector_SAFT_1(y,x,k)=s/(round(min(33,x+m))-
                round(max(1,x-m))+1);
            end
        end
        s=0;
    end
end

theta=-0.3120:0.0195:0.3120;
rho=(2000:1:10000)*0.77E-2+62-950*0.77E-2;    % 62 UT tip to fix points,
950 = tip depth measured
[R,T]=meshgrid(rho,theta);
[x,y]=pol2cart(T,R);
%y=y';
HT=Sector_SAFT_1(:, :, 151)';
surf(x,y,HT);

```



```

shading interp;
view(90,90);
cmin=max(max(Sector_SAFT_1(:, :, 151)));
cmax=max(max(Sector_SAFT_1(:, :, 151)));
caxis([cmin cmax]);
%axis([1 128 0 6000]);
figure
surf(x,y,SR_all_n0(2000:10000, :, 151)');
shading interp;
view(90,90);
%caxis([-30 0]);

%I: original image
%A: [1 4 9 ... 78^2]*1.419E-4^2 depth
B=B_4_X; % scanning path matrix
R=(1:1:60)*12.8/60; %
radius matrix % length from
L=45; % phi matrix
fix point to UT tip (units: mm)
phi=atan(R/L);
%theta=-3.1416:6.2832/419:3.1416;

%circular SAFT
g=1:8192;
A=g.^2*(0.77E-2)^2; %units:mm, depth look up table
%R=0.55148/101; % Rotation angle per line (unit:radins)
%L=41.68; % Lenth of scanning radius (unit:mm)
%m=2; % Number of UT sources to be considered
s=0;
%total_index=0;
Circular_SAFT_1=zeros(8192,256,60); %creat zero matrix for result

for k=1:60
%P32SAFT=P32(:, :, k);
I=B_4_X(1:8192, :, k);
background=mean(I(:, 1));
Circular_SAFT_1(:, :, k)=background;
if k<=10
m=10; % neighboring rows 1:10 m=10 10:20
m=7 20:40 m=5 40:50 m=3 50:60 m=2
range=0.00125;
elseif k>10&&k<=20
m=5;
range=0.0025;
elseif k>20&&k<=30
m=5;
range=0.0030;
elseif k>30&&k<=40
m=5;
range=0.0045;
elseif k>40&&k<=50
m=5;

```

```

range=0.0065;
elseif k>50&&k<=60
m=5;
range=0.009;
end

for x=1:1:256                                % target lateral position
    for y=1000:1:1500                          % target depth

        if x-m>0&&x+m<=256
            for i=round(max(1,x-m)):1:round(min(256,x+m))    % total
Vitual Ultrasound sources
                a=0.77E-2*y;
                r=R(k);
                r1=r+a*sin(phi(k));
                theta=(abs(x-i)/256*360/180*3.14);

                d=a^2*cos(phi(k))^2+r^2+r1^2-2*r*r1*cos(theta);    % 2000-
950=1050, cos theory, a^2+b^2-2abcos(theta)=d^2
                [c,j]=min(abs(sqrt(A)-sqrt(d)));

                if c>range                                % 1:10 c=0.0005 10:20 c=0.001
20:40 c=0.005 40:50 c=0.025 50:60 c=0.05
                    s=s+background;

                else
                    s=s+I(j,i);
                end
                %Circular_SAFT_1(y,x,k)=s/(round(min(256,x+m))-
round(max(1,x-m))+1);

                % s=0;
            end
        elseif x-m<=0
            for i=1:1:x+m    % total Vitural Ultrasound sources
                a=0.77E-2*y;
                r=R(k);
                r1=r+a*sin(phi(k));
                theta=(abs(x-i)/256*360/180*3.14);

                d=a^2*cos(phi(k))^2+r^2+r1^2-2*r*r1*cos(theta);    % 2000-
950=1050, cos theory, a^2+b^2-2abcos(theta)=d^2
                [c,j]=min(abs(sqrt(A)-sqrt(d)));

                if c>range                                % 1:10 c=0.0005 10:20 c=0.001
20:40 c=0.005 40:50 c=0.025 50:60 c=0.05
                    s=s+background;

                else
                    s=s+I(j,i);
                end
            end
        end
    end
end

```

```

    for i=256-m+x:1:256
        d=a^2*cos(phi(k))^2+r^2+r1^2-2*r*r1*cos(theta); % 2000-
950=1050, cos theory, a^2+b^2-2abcos(theta)=d^2
        [c,j]=min(abs(sqrt(A)-sqrt(d)));

        if c>range % 1:10 c=0.0005 10:20 c=0.001
20:40 c=0.005 40:50 c=0.025 50:60 c=0.05
            s=s+background;

        else
            s=s+I(j,i);
        end
        % Circular_SAFT_1(y,x,k)=s/(2*m+1);

        % s=0;
    end
elseif x+m>256

    for i=x-m:256 % total Vitural Ultrasound sources
        a=0.77E-2*y;
        r=R(k);
        r1=r+a*sin(phi(k));
        theta=(abs(x-i)/256*360/180*3.14);

        d=a^2*cos(phi(k))^2+r^2+r1^2-2*r*r1*cos(theta); % 2000-
950=1050, cos theory, a^2+b^2-2abcos(theta)=d^2
        [c,j]=min(abs(sqrt(A)-sqrt(d)));

        if c>range % 1:10 c=0.0005 10:20 c=0.001
20:40 c=0.005 40:50 c=0.025 50:60 c=0.05
            s=s+background;

        else
            s=s+I(j,i);
        end

    end
    for i=1:1:x-256+m % total Vitural Ultrasound sources
        a=0.77E-2*y;
        r=R(k);
        r1=r+a*sin(phi(k));
        theta=(abs(x-i)/256*360/180*3.14);

        d=a^2*cos(phi(k))^2+r^2+r1^2-2*r*r1*cos(theta); % 2000-
950=1050, cos theory, a^2+b^2-2abcos(theta)=d^2
        [c,j]=min(abs(sqrt(A)-sqrt(d)));

        if c>range % 1:10 c=0.0005 10:20 c=0.001
20:40 c=0.005 40:50 c=0.025 50:60 c=0.05
            s=s+background;

```

```

else
    s=s+I(j,i);
end
%Circular_SAFT_1(y,x,k)=s/(2*m+1);

    %s=0;
end
end
Circular_SAFT_1(y,x,k)=s/(2*m+1);

    s=0;
end
for y=3700:1:4350                % target depth

    if x-m>0&&x+m<=256
    for i=round(max(1,x-m)):1:round(min(256,x+m))    % total
Vitual Ultrasound sources
        a=0.77E-2*y;
        r=R(k);
        r1=r+a*sin(phi(k));
        theta=(abs(x-i)/256*360/180*3.14);

        d=a^2*cos(phi(k))^2+r^2+r1^2-2*r*r1*cos(theta);    % 2000-
950=1050, cos theory, a^2+b^2-2abcos(theta)=d^2
        [c,j]=min(abs(sqrt(A)-sqrt(d)));

        if c>range                % 1:10 c=0.0005 10:20 c=0.001
20:40 c=0.005 40:50 c=0.025 50:60 c=0.05
            s=s+background;

        else
            s=s+I(j,i);
        end
        %Circular_SAFT_1(y,x,k)=s/(round(min(256,x+m))-
round(max(1,x-m))+1);

        % s=0;
    end
elseif x-m<=0
for i=1:1:x+m                % total Vitural Ultrasound sources
        a=0.77E-2*y;
        r=R(k);
        r1=r+a*sin(phi(k));
        theta=(abs(x-i)/256*360/180*3.14);

        d=a^2*cos(phi(k))^2+r^2+r1^2-2*r*r1*cos(theta);    % 2000-
950=1050, cos theory, a^2+b^2-2abcos(theta)=d^2
        [c,j]=min(abs(sqrt(A)-sqrt(d)));

        if c>range                % 1:10 c=0.0005 10:20 c=0.001
20:40 c=0.005 40:50 c=0.025 50:60 c=0.05
            s=s+background;

```

```

else
    s=s+I(j,i);
end
end
for i=256-m+x:1:256
    d=a^2*cos(phi(k))^2+r^2+r1^2-2*r*r1*cos(theta); % 2000-
950=1050, cos theory, a^2+b^2-2abcos(theta)=d^2
    [c,j]=min(abs(sqrt(A)-sqrt(d)));

    if c>range % 1:10 c=0.0005 10:20 c=0.001
20:40 c=0.005 40:50 c=0.025 50:60 c=0.05
        s=s+background;

    else
        s=s+I(j,i);
    end
    % Circular_SAFT_1(y,x,k)=s/(2*m+1);

    % s=0;
end
elseif x+m>256

for i=x-m:256 % total Vitural Ultrasound sources
    a=0.77E-2*y;
    r=R(k);
    r1=r+a*sin(phi(k));
    theta=(abs(x-i)/256*360/180*3.14);

    d=a^2*cos(phi(k))^2+r^2+r1^2-2*r*r1*cos(theta); % 2000-
950=1050, cos theory, a^2+b^2-2abcos(theta)=d^2
    [c,j]=min(abs(sqrt(A)-sqrt(d)));

    if c>range % 1:10 c=0.0005 10:20 c=0.001
20:40 c=0.005 40:50 c=0.025 50:60 c=0.05
        s=s+background;

    else
        s=s+I(j,i);
    end

end
for i=1:1:x-256+m % total Vitural Ultrasound sources
    a=0.77E-2*y;
    r=R(k);
    r1=r+a*sin(phi(k));
    theta=(abs(x-i)/256*360/180*3.14);

    d=a^2*cos(phi(k))^2+r^2+r1^2-2*r*r1*cos(theta); % 2000-
950=1050, cos theory, a^2+b^2-2abcos(theta)=d^2
    [c,j]=min(abs(sqrt(A)-sqrt(d)));

```

```

                if c>range                                % 1:10 c=0.0005 10:20 c=0.001
20:40 c=0.005 40:50 c=0.025 50:60 c=0.05
                    s=s+background;

                else
                    s=s+I(j,i);
                end
                %Circular_SAFT_1(y,x,k)=s/(2*m+1);

                %s=0;
            end
            end
            Circular_SAFT_1(y,x,k)=s/(2*m+1);

            s=0;
        end
    end

    %generate 2D images for 3D reconstruction
    theta=-3.14:6.28/419:3.14;
    rho=(0:1:15)*1.54;
    C=zeros(1,420);

    for i=1:8192
        for j=1:16
            %Bname=sprintf('BR_%d',B(j));
            C(j,1:420)=SR_SAFT(i,1+420*(j-1):420*j);
        end
        CT=C';
        [R,T]=meshgrid(rho,theta);
        [x,y]=pol2cart(T,R);
        surf(x,y,CT);
        set(gcf, 'color', 'w');
        shading interp
        view(-90,90)
        axis equal
        axis off
        grid off
        cmin=max(max(max(SR_SAFT)));
        cmax=max(max(max(SR_SAFT)));
        caxis=[cmin, cmax];

        %caxis([-20,-9]);
        %colormap(gray);

        %figure

```

end

```
im = getframe;  
im = imresize(im, cdata, [100 100]);  
fname = sprintf('SAFT%0d.png', i);  
imwrite(im, fname, 'png');  
%imwrite (im, 'yourplot.png', 'png')  
set(gcf, 'Renderer', 'zbuffer');  
%figure('Renderer', 'zbuffer');
```

